

Accurate solutions of wave propagation problems under impact loading by the standard, spectral and isogeometric high-order finite elements. Comparative study of accuracy of different space-discretization techniques

A. Idesman ^{a,*}, D. Pham ^a, J.R. Foley ^b, M. Schmidt ^b

^a Department of Mechanical Engineering, Texas Tech University, Lubbock, TX 79409-1021, USA
^b Air Force Research Laboratory, Munitions Directorate, Eglin Air Force Base, FL 32542, USA



ARTICLE INFO

Article history:

Received 27 September 2013
 Received in revised form
 5 March 2014
 Accepted 14 May 2014
 Available online 7 June 2014

Keywords:

Elastic and acoustics waves
 Finite elements
 Spectral elements
 Isogeometric elements
 Accuracy

ABSTRACT

For the first time, accurate numerical solutions to impact problems have been obtained with the standard, spectral, and isogeometric high-order finite elements. Spurious high-frequency oscillations appearing in numerical results are quantified and filtered out by the two-stage time-integration approach. We also use the 1-D impact problem with a simple analytical solution for the comparison of accuracy of the different space-discretization techniques used for transient acoustics and elastodynamics problems. The numerical results show the computational efficiency of the linear finite elements with reduced dispersion compared with other space-discretization techniques used for elastodynamics with implicit and explicit time-integration methods. We also show that for all space-discretization methods considered (except the linear finite elements with the lumped mass matrix), very small time increments which are much smaller than stability limit should be used in basic computations at large observation times. We should note that the size of time increments used at the filtering stage and calculated according to the special formulas defines the range of actual frequencies and can be used as a quantitative measure for the comparison and prediction of the accuracy of different space-discretization techniques. We also show that the new findings are valid in the multidimensional case.

© 2014 Elsevier B.V. All rights reserved.

1. Introduction

There are many different space-discretization approaches used for the solution of transient acoustics and elastodynamics problems within the semi-discrete formulations. For these formulations, first a space-discretization method is applied to the corresponding system of partial differential equations and reduces it to a system of ordinary differential equations in time that has the following form:

$$\mathbf{M}\ddot{\mathbf{U}} + \mathbf{C}\dot{\mathbf{U}} + \mathbf{K}\mathbf{U} = \mathbf{R}, \quad (1)$$

where \mathbf{M} , \mathbf{C} , and \mathbf{K} are the mass, damping, and stiffness matrices, respectively, \mathbf{U} is the vector of the nodal displacement, \mathbf{R} is the vector of the nodal load. In this paper, we will consider the space-discretization based on the standard low- and high-order finite elements (e.g., see [1–3] and others), the linear and quadratic finite

elements with reduced dispersion (e.g., see [4–10] and others), the spectral elements (e.g., see [11–15] and others) and the isogeometric elements (e.g., see [16–19] and others). Of course, there are many other space-discretization methods that can be used for elastodynamics problems such as the boundary element method (e.g., see [20]), different meshless methods (e.g., see [21–26]), the smoothed FEM (e.g., see [27,28]) and many others. The selection of the space discretization methods used in this paper is explained by their popularity as well as by the availability of the corresponding computer codes. For example, the standard high-order finite elements are implemented in the commercial finite-element code “COMSOL”, the spectral low- and high-order elements are implemented into the code “SEMLAB” (see the website “<http://www.gps.caltech.edu/~ampuero/software.html>”), the isogeometric elements are implemented into the code “IGAFEM” (see the website “<http://sourceforge.net/projects/cmcodes/>”); we implemented the linear and quadratic finite elements with reduced dispersion into the finite element code “FEAP”; see [3].

The application of time-integration methods to Eq. (1) yields the numerical solutions of transient acoustics or elastodynamics

* Corresponding author. Tel.: +1 806 742 3563; fax: +1 806 742 3540.
 E-mail address: alexander.idesman@ttu.edu (A. Idesman).

problems. These numerical results contain the space- and time-discretization errors. In the present paper, first we will study the space-discretization error introduced by different space-discretization techniques. In order to exclude the time-discretization error, we will select very small time increments at which the numerical solutions are practically independent of the size of time increments and are close to the exact solution of Eq. (1). It is known that the space-discretization error for elastodynamics problems is related to “the pollution effect” (e.g., see [29–31]) and the numerical dispersion error. Therefore, the analytical study of the numerical dispersion error is very often used in the literature for the comparison of different space-discretization techniques; e.g., see [6–9,32–36] and many others. We should mention that the analytical study of the dispersion error is difficult for high-order space-discretization methods. Moreover, the analysis of the dispersion error based on the Helmholtz equation does not consider the effect of the observation time and time increments on the accuracy of transient elastodynamics problems; however, this effect is very significant (see Section 3 below). In contrast to the study of the numerical dispersion error for the selected frequency in the Helmholtz equation, in many cases we are interested in the combined effect of a range of frequencies on the accuracy of numerical results obtained by different space-discretization techniques. This analysis can be done by the comparison of the accuracy of numerical solutions of the benchmark elastodynamics problems for which a wide range of frequencies is excited simultaneously. There is a very limited number of such benchmark elastodynamics problems with known analytical solutions. The issue is also due to the presence of spurious high-frequency oscillations in numerical solutions for transient acoustics and elastodynamics problems that makes numerical results very inaccurate. Despite a large number of publications related to the treatment of spurious oscillations, this issue has not been resolved in the literature. We would like to mention few recent papers [37–40] dealing with the reduction of spurious oscillations for elastodynamics problems for the linear and quadratic finite elements. However, even for the standard low-order finite elements, the techniques in [37–40] cannot remove all spurious oscillations and may yield inaccurate results at long-term integration. We should mention that it is difficult to predict and estimate the amplitudes of the spurious oscillations which are excited by the initial and boundary conditions and which depend also on the observation time (e.g., for the same space mesh, the amplitudes of spurious oscillations can become much larger with the increase in the observation time; see Section 3 below). For example, due to the spurious oscillations we have not seen in the literature the accurate numerical solutions of elastodynamics problems at impact loading (or high-frequency loading) for the spectral and isogeometric elements as well as for the standard high-order finite elements. We will resolve this issue by the application of the two-stage time-integration approach recently developed in our papers; e.g., see [5,41,42] and will show that this approach can be effectively used with any space-discretization method.

In the present study, first we accurately solve the 1-D impact elastodynamics problem by the application of the two-stage time-integration technique consisting of the stage of basic computations and the filtering stage. The 1-D impact problem has the following important features: (a) all low- and high-frequencies of the semi-discrete system, Eq. (1), are excited for this problem and (b) the problem has a very simple analytical solution and, therefore, the comparison of the accuracy of the numerical solutions to this problem is easy when the spurious oscillations are removed. In Section 2 we shortly introduce different space-discretization techniques such as the standard low- and high-order finite elements, the spectral elements, the isogeometric elements and the linear and quadratic finite elements with reduced dispersion. Then, in Sections 3.1 and 3.2 we accurately solve the 1-D impact

problem using different space-discretization methods as well as the implicit and explicit time-integration methods with very small time increments in basic computations. Using the accurate numerical solutions to the 1-D impact problem, we compare the accuracy of different space-discretization techniques. We also show that the size of time increments used for the filtering of spurious oscillations at the filtering stage of the two-stage time-integration technique can be used as a quantitative measure for the comparison and prediction of the accuracy of different space-discretization approaches. In Section 3.3 we analyze the effect of the size of time increments used in basic computations on the accuracy of numerical solutions obtained with different space-discretization techniques. According to our results, the typical statement in finite element textbooks, that for explicit methods a time increment should be close to the stability limit (e.g., see [1,43]), is not true, because the size of a time increment should depend on the observation time and should be much smaller than the stability limit at large observation times. In Section 4 we solve a 2-D transient acoustics problem and show that the findings of the paper are also valid in the multidimensional case. The recently developed two-stage time-integration approach with the stage of basic computations and the filtering stage is shortly summarized in the Appendix.

We would also like to emphasize that despite a large number of different space-discretization techniques for elastodynamics problems, it is very often unclear what the best technique is. There are many factors that can affect the selection of the best method such as accuracy, computation costs, the simplicity of implementation and many others. In this paper we also estimate the computational efficiency of different space-discretization techniques for elastodynamics. We compare their computational costs for the solution of the 1-D impact problem at the same accuracy. Because for this problem all frequencies of the structure are excited and affect the accuracy, we believe that the solution to this problem can serve as the performance benchmark for different space-discretization techniques for elastodynamics.

2. Standard low- and high-order finite elements, spectral and isogeometric elements, finite elements with reduced dispersion

The application of a space-discretization method to elastodynamics problems leads to the semi-discrete equations (1). Formally, for the space-discretization techniques considered in the paper, the calculation of the mass and stiffness matrices can be represented by the classical finite element equations as follows:

$$\mathbf{M} = \sum_e \mathbf{M}^e, \quad \mathbf{K} = \sum_e \mathbf{K}^e \quad (2)$$

where the global mass \mathbf{M} and stiffness \mathbf{K} matrices have a banded structure (the dimensions of these matrices for different space-discretization techniques will be discussed below in Section 3) and are obtained by the summation of the corresponding local (element) matrices \mathbf{M}^e and \mathbf{K}^e :

$$\begin{aligned} \mathbf{M}^e &= \rho A \int_{-1}^1 \mathbf{N}^T(s) \mathbf{N}(s) \det(\mathbf{J}(s)) ds \\ &\approx \rho A \sum_{i=1}^{m_1} w_i \mathbf{N}^T(\alpha_M^i) \mathbf{N}(\alpha_M^i) \det(\mathbf{J}(\alpha_M^i)), \end{aligned} \quad (3)$$

$$\begin{aligned} \mathbf{K}^e &= A \int_{-1}^1 E \left[\frac{\partial \mathbf{N}(s)}{\partial x} \right]^T \left[\frac{\partial \mathbf{N}(s)}{\partial x} \right] \det(\mathbf{J}) ds \\ &\approx \sum_{i=1}^{m_2} A E w_i \left[\frac{\partial \mathbf{N}(\alpha_K^i)}{\partial x} \right]^T \left[\frac{\partial \mathbf{N}(\alpha_K^i)}{\partial x} \right] \det(\mathbf{J}(\alpha_K^i)) \end{aligned} \quad (4)$$

Here, Eqs. (3) and (4) are given for the 1-D case, E is Young's modulus, ρ is the density, A is the cross-sectional area of an element, \mathbf{N} and $\partial\mathbf{N}/\partial x$ are the shape matrix and its derivative with respect to the physical coordinate x ; s is the parametric coordinate ($-1 \leq s \leq 1$ for each element); α_M^i and α_K^i are the coordinates of integration points in the parametric space for the integration rule used; w_i are the weights for the selected integration rule; m_1 and m_2 are the numbers of integration points for the numerical integration of the mass and stiffness matrices (generally, different integration rules and the number of integration points can be used for the numerical integration of these matrices). The elements of the shape matrix \mathbf{N} in Eq. (3) are the polynomial shape functions for all space-discretization techniques considered in the paper. For example, the standard low- and high-order finite elements are based on the uniform spacing of internal nodes within the element and the Lagrange polynomials $p_j(s)$ of degree N ($j = 1, 2, \dots, N$ where $N+1$ is the number of nodes in an element).

For the spectral high-order elements with $N \geq 3$ (there is no difference between the standard finite elements and the spectral elements for $N \leq 2$), the Lagrange polynomials $p_j(s)$ of degree N and the non-uniform spacing of internal nodes within the element are used; the coordinates s_k ($s_k \in [-1, 1]$ with $k = 1, 2, \dots, N+1$) of the nodes in the parametric space are the Gauss–Lobatto–Legendre points which are the $(N + 1)$ roots of the following equation:

$$(1 - s_k^2)p'_N(s_k) = 0, \quad (5)$$

where $p'_N(s)$ is the derivative of the Legendre polynomial of degree N ; e.g., see [15]. It can also be shown that the application of the Gauss–Lobatto–Legendre integration rule with $N+1$ integration points yields an approximate value of the mass matrix in Eq. (3) for the spectral elements and this approximate mass matrix is diagonal for any order of an element (e.g., see [15]).

In contrast to the standard finite elements and the spectral elements based on the piecewise-polynomial approximation of a numerical solution in the 1-D space (the derivatives of this solution are discontinuous across the element boundaries), the isogeometric elements allow the continuous derivatives of the numerical solution across the element boundaries. The shape functions for the isogeometric elements are based on the polynomial B-splines in the 1-D case; e.g., see [16–19].

The semi-discrete equations for the linear and quadratic finite elements with reduced dispersion can be easily obtained by the use of the global consistent \mathbf{M}^{cons} and lumped \mathbf{M}^{lump} mass matrices for the standard finite elements. For implicit time integration methods, the mass matrix \mathbf{M} in Eq. (1) should be replaced in this case by a weighted average mass matrix $\mathbf{M} = \mathbf{M}^{lump}\gamma + \mathbf{M}^{cons}(1-\gamma)$ where $\gamma = 0.5$ (see [6,10,44]) for the linear elements and $\gamma = 2/3$ (see [10]) for the quadratic elements. For explicit time-integration methods and the linear elements with reduced dispersion, Eq. (1) can be modified as follows:

$$\mathbf{M}^{lump}\ddot{\mathbf{U}} + \mathbf{M}[\mathbf{M}^{lump}]^{-1}\mathbf{K}\mathbf{U} = \mathbf{M}[\mathbf{M}^{lump}]^{-1}\mathbf{R} \quad (6)$$

where $\mathbf{M} = \mathbf{M}^{lump}\gamma + \mathbf{M}^{cons}(1-\gamma)$ with $\gamma = (3 - \bar{\tau}^2)/2$ and the Courant number $\bar{\tau} = c_0\Delta t/dx$ (Δt is the size of a time increment, dx is the size of a linear finite element, $c_0 = \sqrt{E/\rho}$ is the wave velocity); see [4].

The computational efficiency of a numerical technique for elastodynamics depends on the type (implicit or explicit) of a time-integration method used. Therefore, we will separately compare the numerical techniques with the diagonal mass matrices and explicit time-integration methods (they do not require the solution of a system of algebraic equations) and the numerical techniques with the non-diagonal mass matrices and implicit time-integration methods (they include the solution of a

system of algebraic equations). To summarize, we will accurately solve wave propagation problems and compare the accuracy of the following space-discretization techniques:

- Standard finite elements from the 1st to the 5th order with the consistent mass matrix and implicit time integration methods.
- Isogeometric elements of the 2nd and 3rd orders with the consistent mass matrix and implicit time integration methods.
- Linear and quadratic finite elements with reduced dispersion with the averaged mass matrix and implicit time integration methods.
- Spectral elements from the 1st to the 10th order with the lumped mass matrix and explicit time integration methods.
- Linear finite elements with reduced dispersion with the diagonal mass matrix (see Eq. (6)) and explicit time integration methods.

3. Accurate numerical solutions of the 1-D impact of an elastic bar against a rigid wall

Here, we will accurately solve the 1-D impact problem and will compare the computational efficiency of the different space-discretization techniques for elastodynamics (listed in Section 2). The exact solution of the semi-discrete equations (Eq. (1)) for the 1-D impact problem contains spurious high-frequency oscillations in velocities and stresses; see [41,42,45] and the numerical results after basic computations presented below. Therefore, the two-stage time-integration procedure with the basic computations and the filtering stage (that has been recently developed in our papers [5,42,46] and shortly summarized in the Appendix) is used to obtain accurate and non-oscillatory numerical solutions. For the results presented in this section, we use the implicit trapezoidal rule (for the techniques with the non-diagonal mass matrix) and the explicit central difference method (for the techniques with the diagonal mass matrix) for the time integration in basic computations. In Sections 3.1 and 3.2, very small time increments will be applied for the implicit and explicit methods in basic computations. For very small time increments, the error in time is much smaller than the space-discretization error and can be neglected (in this case the numerical solution in basic computations is close to the exact solution of the semi-discrete equations (1)) and is independent of a time-integration method used). In Section 3.3 we will numerically study the effect of the size of time increments in the basic computations on the accuracy of the results obtained by different space-discretization techniques.

Below, the impact of an elastic bar of the length $L=4$ and the cross section $A=1$ against a rigid wall is considered in the 1-D case (see Fig. 1). Young's modulus is chosen to be $E=1$ and the density to be $\rho=1$. The following boundary conditions are applied: the displacement $u(0, t) = t$ (which corresponds to the velocity $v(0, t) = v_0 = 1$) and $u(4, t) = 0$ (which corresponds to the velocity $v(4, t) = 0$). Initial displacements and velocities are zero; i.e., $u(x, 0) = v(x, 0) = 0$. The analytical solution to this problem for time $0 \leq t \leq L\sqrt{\rho/E} = 4$ includes the continuous variation of

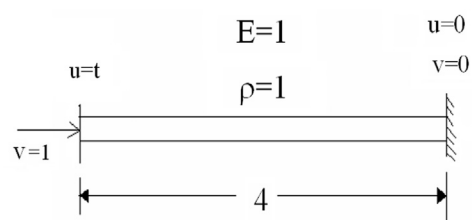


Fig. 1. Impact of an elastic bar of length $L=4$ against a rigid wall.

displacements $u_a(x, t) = t - x$ for $t \geq x$ and $u_a(x, t) = 0$ for $t \leq x$, and the piecewise constant variation of velocities and stresses $v_a(x, t) = -\sigma^a(x, t) = 1$ for $t \geq x$ and $v_a(x, t) = \sigma^a(x, t) = 0$ for $t \leq x$ (at the interface $x=t$, jumps in stresses and velocities occur). For time $4 \leq t \leq 8$ the solution is similar to that for $0 \leq t \leq 4$ with the difference that the elastic wave reflects from the right end and propagates to the left. For time $8 \leq t \leq 12$ the solution is the same as for time $0 \leq t \leq 4$ and so on. In order to compare the results at short- and long-term integrations, the observation times are chosen to be $T = 2; 18; 98; 194$. At these observation times, the exact distributions of the velocities and stresses along the bar are the same and correspond to the location of the wave front in the middle of the bar.

3.1. Space-discretization techniques with the non-diagonal mass matrix

Here, we will solve the 1-D impact problem using the standard low- and high-order finite elements (up to the 5th-order), the isogeometric 2nd- and 3rd-order elements, and the linear and quadratic elements with reduced dispersion. For all these space-discretization methods, the non-diagonal mass matrices and the implicit trapezoidal rule with very small time increments in basic computations are used. Uniform meshes with 101 degrees of freedom (dof) are used for all types of elements (except the standard 3rd-order elements with 100 dof); see Figs. 2–12. In addition to these meshes, we also use uniform meshes with 201 and 251 dof for the linear elements with reduced dispersion; see Figs. 11 and 12. For the isogeometric elements we use uniformly spaced control points as suggested in [18]. Figs. 2–9 show the numerical solutions for the velocity at different observation times. All space-discretization methods yield spurious oscillations after basic computations and the amplitudes of these oscillations increase with the increase in the observation time; see Figs. 2a,b–9a,b. The slope of the wave front in the basic

computations is steeper for short observation times and is more diffusive for large observation times. The filtering stage removes the spurious oscillations. However, despite the same analytical solutions at the selected observation times, the numerical results after the filtering stage are more accurate for short observation times than those for large observation times; see Figs. 2c,d–9c,d. Because the error in time is very small in these calculations and can be neglected, the difference in the numerical results for the same space-discretization method at different observation times is due to the space-discretization error (which is also related to the dispersion error). This difference is smaller for higher-order elements compared with lower-order elements (the dispersion error for higher-order elements is smaller). Fig. 10 compares the numerical results after the filtering stage for the linear and quadratic elements with reduced dispersion at different observation times. As can be seen from Fig. 10, the linear elements are more accurate at the short observation time $T=2$ (see curves 2 and 3 in (a)) and yield approximately the same results as the quadratic elements at the intermediate time $T=18$ (see curves 4 and 5 in (a)). At the large observation times $T=98$ and $T=194$, the quadratic elements with reduced dispersion are more accurate than the linear elements with reduced dispersion (see curves 2–5 in (b)). It is interesting to note that for the numerical results in Fig. 10, the time discretization error is small (due to very small time increments) and can be neglected, as well as the order of the dispersion error is smaller for the quadratic elements compared with that for the linear elements with reduced dispersion (see [10] and the Remark below). This means that the order of the dispersion error is not the only factor describing the space-discretization error in Fig. 10. Comparing the linear and quadratic elements with reduced dispersion in Fig. 10 we can conclude that the effect of the dispersion error becomes more significant at large observation times.

Remark. For very small time increments, the time-discretization error can be neglected and the dispersion error can be determined

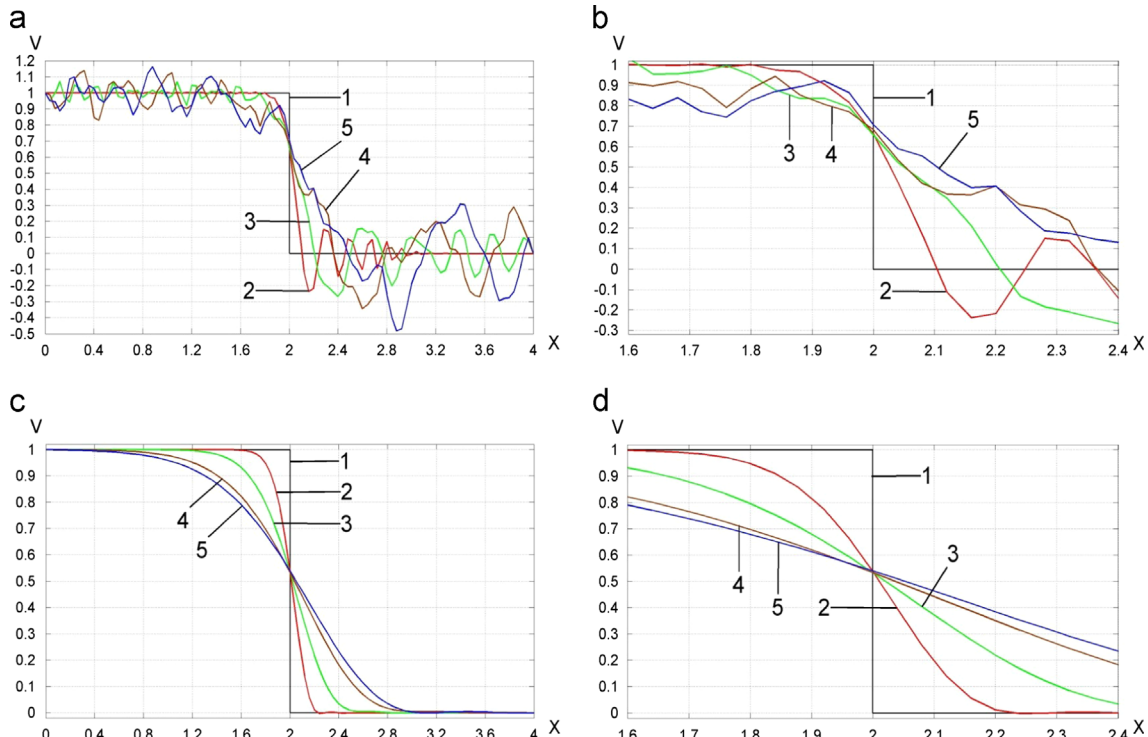


Fig. 2. The velocity distribution along the bar after (a, b) basic computations (the consistent mass matrix and small time increments) and after (c, d) post-processing. A uniform mesh with the standard linear elements and 101 dof is used. Curves 1 correspond to the analytical solutions. Curves 2, 3, 4 and 5 correspond to the observation times $T = 2, 18, 98$ and 194 , respectively. (b) and (d) show the zoomed graphs (a) and (c) in the range $1.6 < x < 2.4$.

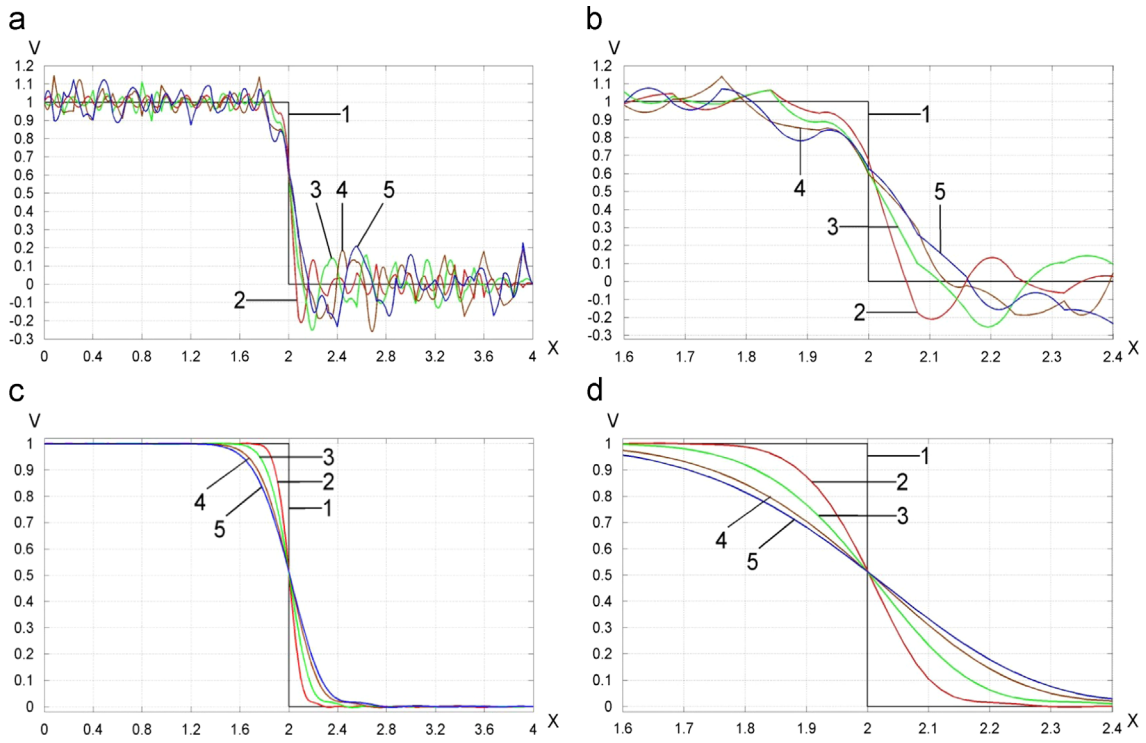


Fig. 3. The velocity distribution along the bar after (a, b) basic computations (the consistent mass matrix and small time increments) and after (c, d) post-processing. A uniform mesh with the standard quadratic elements and 101 dof is used. Curves 1 correspond to the analytical solutions. Curves 2, 3, 4 and 5 correspond to the observation times $T = 2, 18, 98$ and 194 , respectively. (b) and (d) show the zoomed graphs (a) and (c) in the range $1.6 < x < 2.4$.

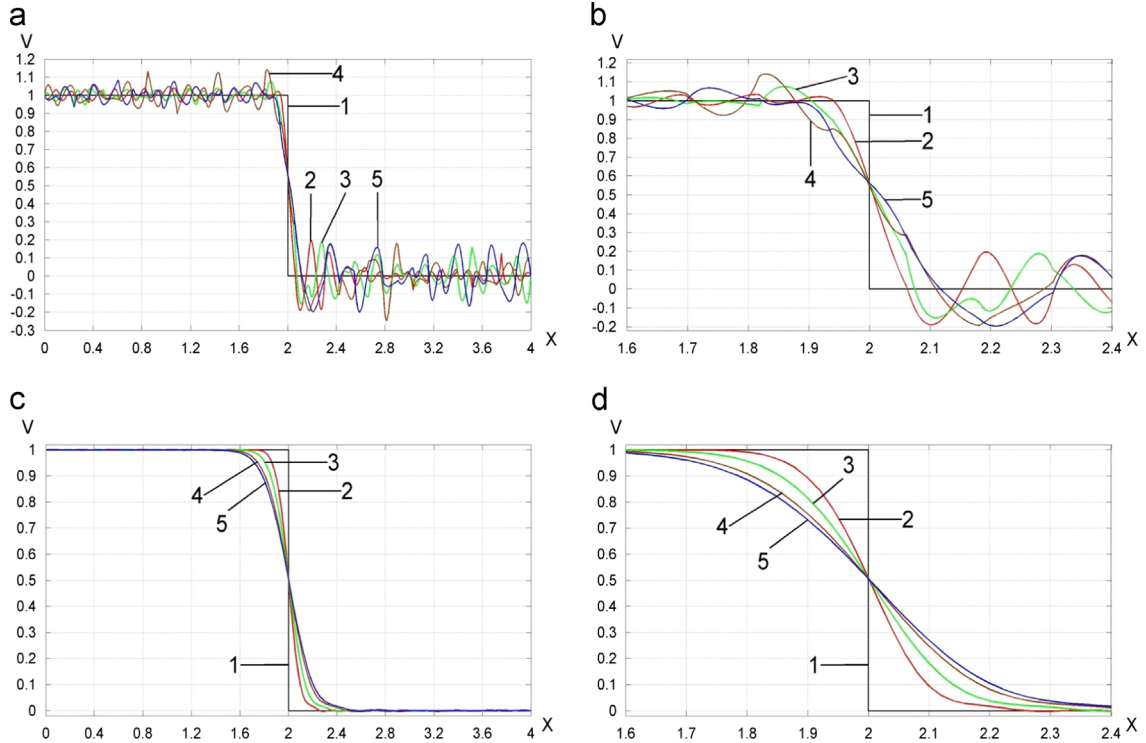


Fig. 4. The velocity distribution along the bar after (a, b) basic computations (the consistent mass matrix and small time increments) and after (c, d) post-processing. A uniform mesh with the standard 3rd-order elements and 100 dof is used. Curves 1 correspond to the analytical solutions. Curves 2, 3, 4 and 5 correspond to the observation times $T = 2, 18, 98$ and 194 , respectively. (b) and (d) show the zoomed graphs (a) and (c) in the range $1.6 < x < 2.4$.

using the Helmholtz equation. For example, the leading term in the dispersion error in this case is (see 10): $\Omega^3(2\gamma-1)/24$, $\Omega^5(3\gamma-2)/2880$, $\Omega^7(4\gamma-3)/604,800$ for the linear, quadratic and

cubic elements where $\gamma = 0$ for the standard finite elements and $\gamma = 1$ for the spectral finite elements (see below Section 3.2 for the numerical examples) as well as $\Omega^5/480$, $32\Omega^7/2,419,200$ and

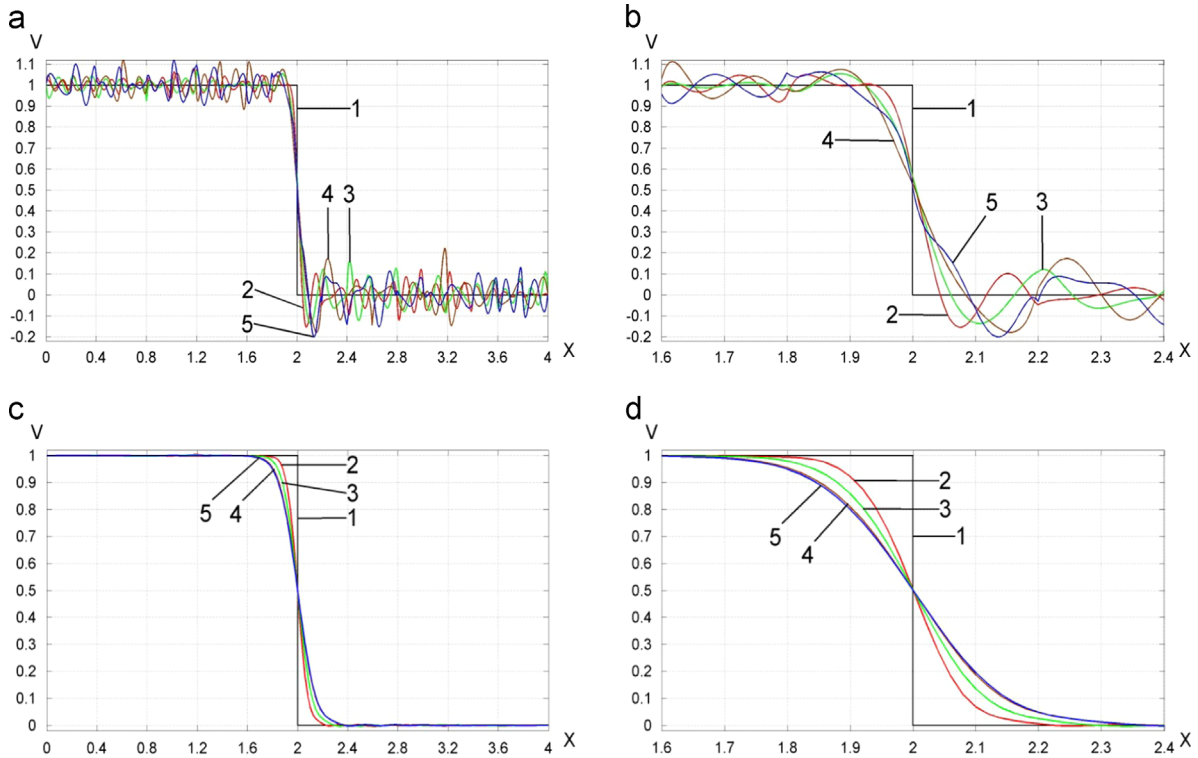


Fig. 5. The velocity distribution along the bar after (a, b) basic computations (the consistent mass matrix and small time increments) and after (c, d) post-processing. A uniform mesh with the standard 5th-order elements and 101 dof is used. Curves 1 correspond to the analytical solutions. Curves 2, 3, 4 and 5 correspond to the observation times $T = 2, 18, 98$ and 194 , respectively. (b) and (d) show the zoomed graphs (a) and (c) in the range $1.6 < x < 2.4$.

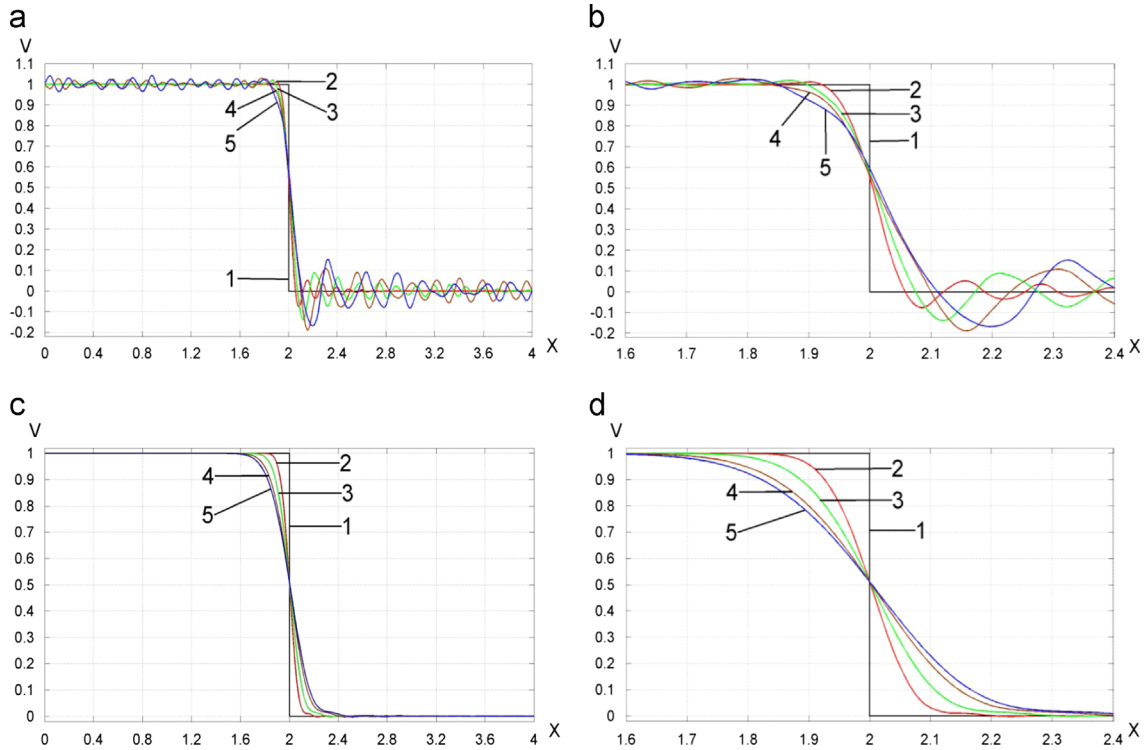


Fig. 6. The velocity distribution along the bar after (a, b) basic computations (the consistent mass matrix and small time increments) and after (c, d) post-processing. A uniform mesh with the isogeometric quadratic elements and 101 dof is used. Curves 1 correspond to the analytical solutions. Curves 2, 3, 4 and 5 correspond to the observation times $T = 2, 18, 98$ and 194 , respectively. (b) and (d) show the zoomed graphs (a) and (c) in the range $1.6 < x < 2.4$.

$\Omega^9/31,752,000$ for the linear, quadratic and cubic elements with reduced dispersion where $\Omega = \omega h$ with frequency ω and the element size h .

Fig. 11 compares the numerical results for the standard low- and high-order finite elements at time $T=18$. As can be seen, at the same number of dof, the increase in the order of the standard

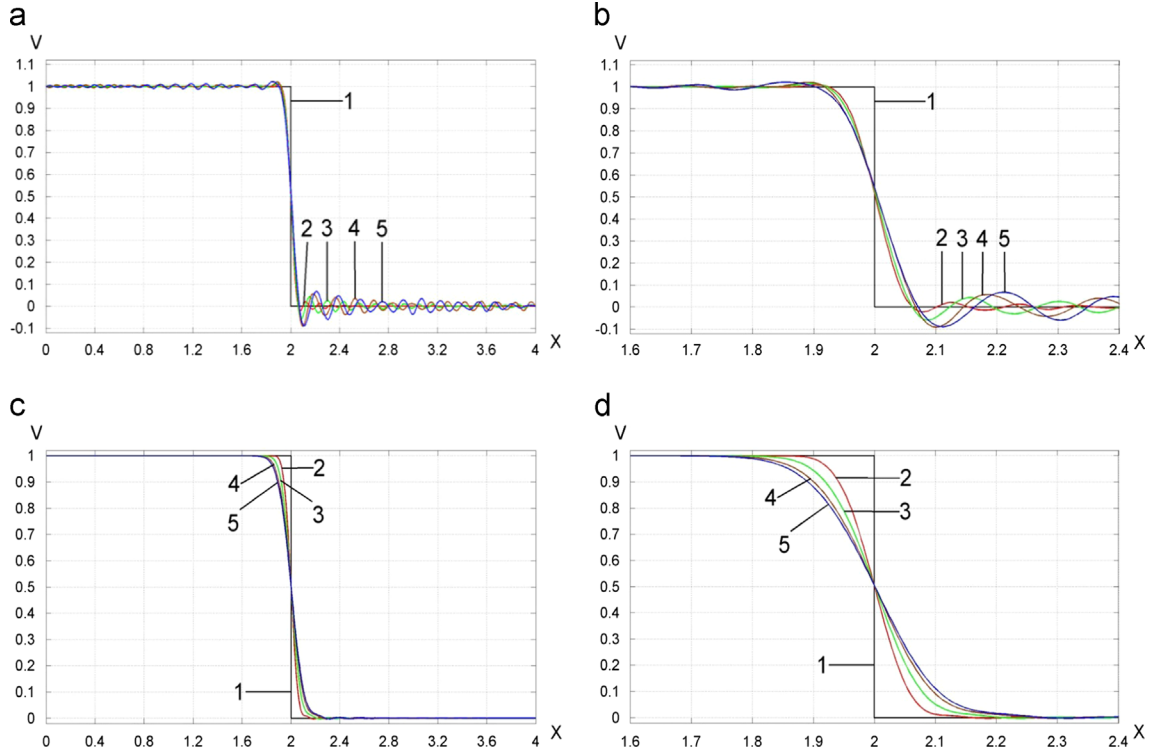


Fig. 7. The velocity distribution along the bar after (a, b) basic computations (the consistent mass matrix and small time increments) and after (c, d) post-processing. A uniform mesh with the isogeometric 3rd-order elements and 101 dof is used. Curves 1 correspond to the analytical solutions. Curves 2, 3, 4 and 5 correspond to the observation times $T = 2, 18, 98$ and 194 , respectively. (b) and (d) show the zoomed graphs (a) and (c) in the range $1.6 < x < 2.4$.

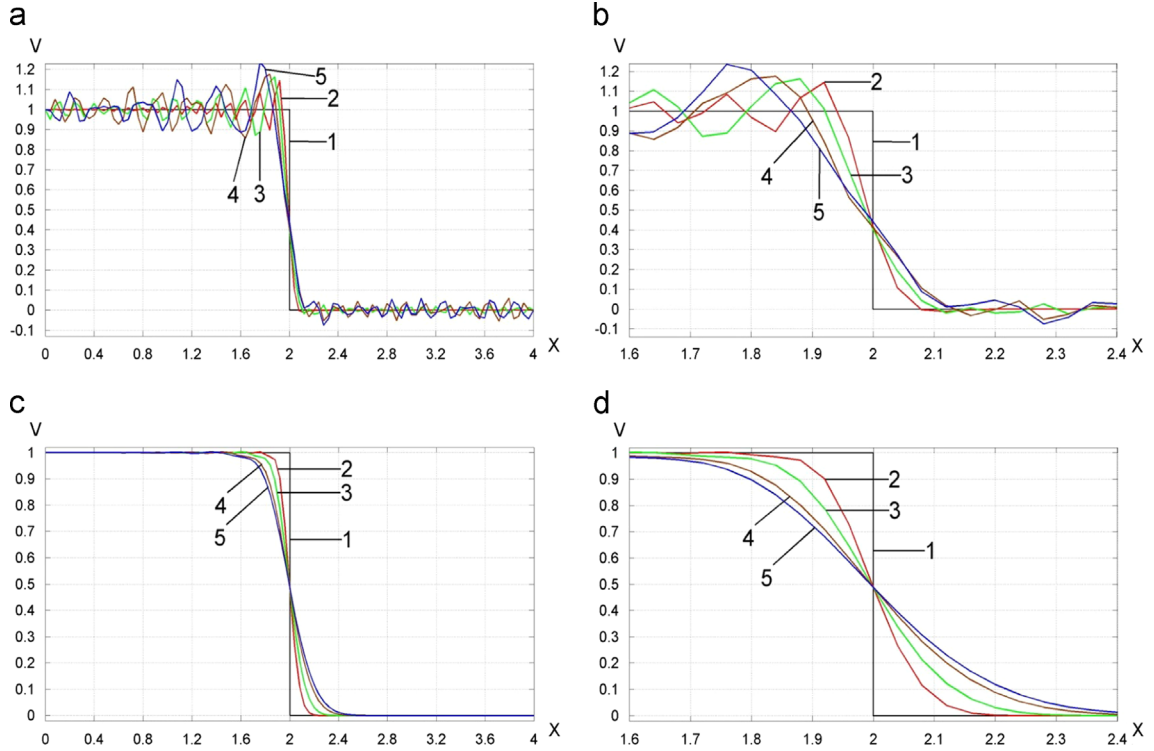


Fig. 8. The velocity distribution along the bar after (a, b) basic computations (the non-diagonal mass matrix and small time increments) and after (c, d) post-processing. A uniform mesh with the linear elements with reduced dispersion and 101 dof is used. Curves 1 correspond to the analytical solutions. Curves 2, 3, 4 and 5 correspond to the observation times $T = 2, 18, 98$ and 194 , respectively. (b) and (d) show the zoomed graphs (a) and (c) in the range $1.6 < x < 2.4$.

finite elements leads to the increase in accuracy. This increase is significant from the transition from the 1st-order to the 2nd-order finite elements (see curves 2 and 3 in Fig. 11a,b) and is much smaller from the transition from the 2nd- to the 3rd-order finite

elements and so on (see curves 3–5 in Fig. 11a,b). At the same number of dof, the calculations with higher-order elements lead to a greater computation cost (e.g., due to a greater bandwidth of the finite-element matrices for higher-order elements). Therefore, the

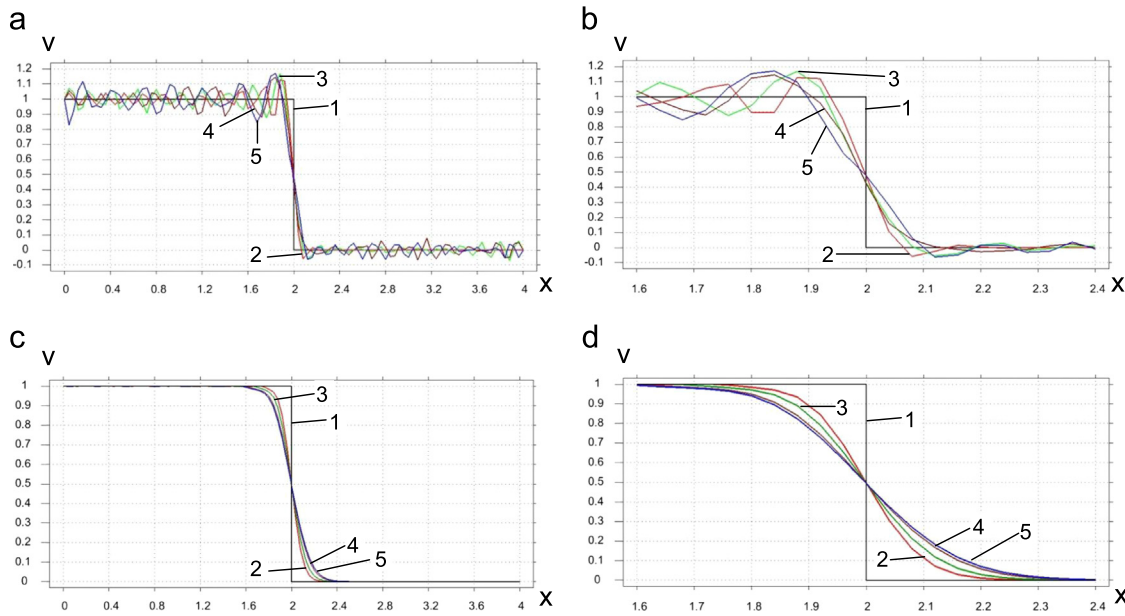


Fig. 9. The velocity distribution along the bar after (a, b) basic computations (the non-diagonal mass matrix and small time increments) and after (c, d) post-processing. A uniform mesh with the quadratic elements with reduced dispersion and 101 dof is used. Curves 1 correspond to the analytical solutions. Curves 2, 3, 4 and 5 correspond to the observation times $T = 2, 18, 98$ and 194 , respectively. (b) and (d) show the zoomed graphs (a) and (c) in the range $1.6 < x < 2.4$.

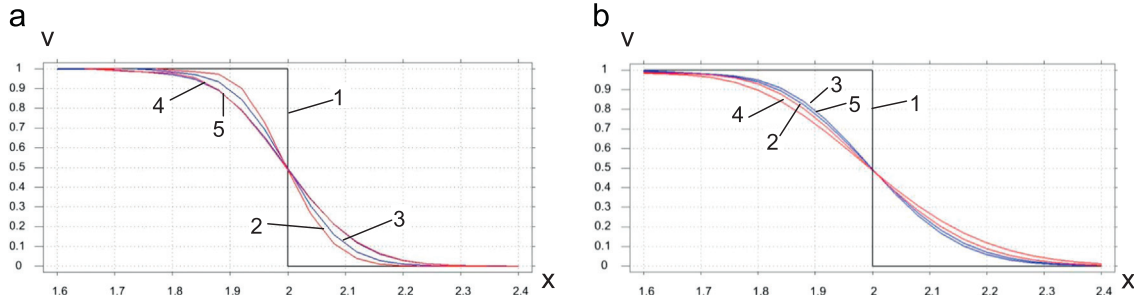


Fig. 10. The velocity distribution along the bar after post-processing. Uniform meshes with the linear (curves 2 and 4) and quadratic (curves 3 and 5) elements with reduced dispersion and 101 dof are used. Curves 1 correspond to the analytical solutions. Curves (2, 3) in (a), (4, 5) in (a), (2, 3) in (b), (4, 5) in (b) correspond to the observation times $T = 2, 18, 98$ and 194 , respectively.

estimation of the computation cost at the same accuracy is necessary in order to select an optimal space-discretization strategy: to use the standard high-order elements or to use the standard low-order elements with a larger number of dof (mesh refinement).

Figs. 11 and 12 compare the accuracy of different space-discretization techniques at times $T=18$ and $T=194$. For all types of elements we have sparse matrices described by the bandwidth b . As can be seen, at the same number $n_1 = 101$ of dof, the isogeometric 3rd-order elements (curves 6) yield the most accurate results (compared with the standard 5th-order elements or the linear elements with reduced dispersion). The results with the standard 3rd-order elements are close to those obtained by the linear elements with reduced dispersion and $n_1 = 101$ dof (see curves 2 and 4 in Fig. 11c,d). However, the results at time $T=18$ obtained by the linear elements with reduced dispersion with $n_2 = 201$ dof (with the bandwidth $b_2 = 3$) are close to those for the isogeometric 3rd-order elements with $n_1 = 101$ dof (with the bandwidth $b_1 = 7$) and are even slightly more accurate; see curves 3 and 6 in Fig. 12a. Implicit time-integration methods with the considered space-discretization techniques include a solution of a system of algebraic equations with the computation cost proportional to nb^2 for the matrix factorization and to nb for the back substitution (n is the number of dof, b is the bandwidth and $n \gg b$). For 1-D uniform meshes, we have $n_1/n_2 \approx 0.5$ and

$b_1/b_2 = 7/3$. This means at the same accuracy at time $T=18$, the linear elements with reduced dispersion and 201 dof require much less computation time compared with the isogeometric 3rd-order elements with 101 dof. We should mention that for the same accuracy, the difference in the computation time between the isogeometric 3rd-order elements and the linear elements with reduced dispersion depends on the observation time. Despite the fact that the isogeometric elements become more accurate at larger observation time compared with other space-discretization techniques (see Fig. 12b), even at the large observation time $T=194$, the linear elements with reduced dispersion are still more computationally efficient than the isogeometric elements. For example, the results obtained at time $T=194$ by the linear elements with reduced dispersion for 251 dof are slightly more accurate and require less computation time compared with the isogeometric 3rd-order elements with 101 dof; see curves 4 and 6 in Fig. 12b. Similarly it can be shown that the linear elements with reduced dispersion are more computationally efficient than the quadratic elements with reduced dispersion even at large computation times presented in Fig. 10b. For example our numerical results show that at the time $T=194$, 130 linear elements ($n_1 = 131$ dof and the bandwidth $b_1 = 3$) with reduced dispersion yields approximately the same results as 100 quadratic elements ($n_2 = 101$ dof and the bandwidth $b_2 = 5$) with reduced dispersion; see curve 5 in Fig. 10b. This means that at the same accuracy the

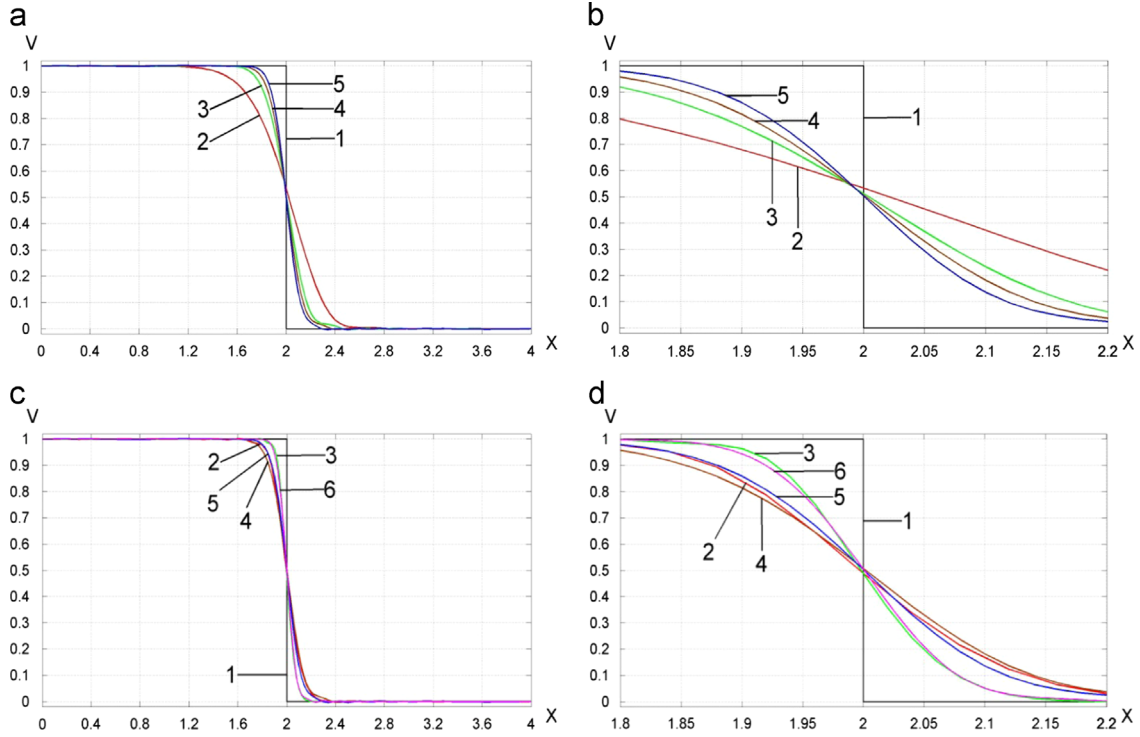


Fig. 11. The velocity distribution along the bar at the observation time $T=18$ after post-processing. We compare the curves from Figs. 2–5, 7 and 8. Curves 1 correspond to the analytical solutions. Curves 2 in (a, b), 3 in (a, b), 4 and 5 correspond to the standard linear, quadratic, 3rd-order (100 dof) and 5th-order elements with 101 dof. Curves 2 in (c, d) and 3 in (c, d) correspond to the linear elements with reduced dispersion (the non-diagonal mass matrix) with 101 and 201 dof, respectively. Curves 6 correspond to the isogeometric 3rd-order elements with 101 dof. (b) and (d) show the zoomed graphs (a) and (c) in the range $1.8 < x < 2.2$.

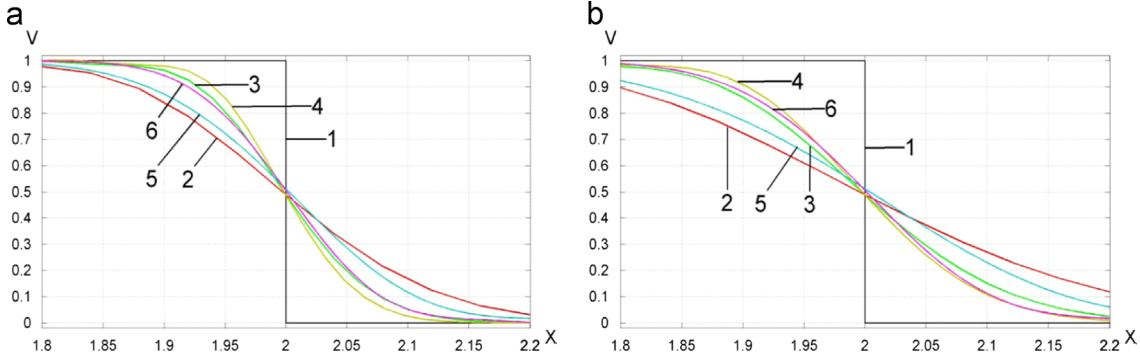


Fig. 12. The velocity distribution along the bar in the range $1.8 < x < 2.2$ at the observation times $T=18$ (a) and $T=194$ (b) after post-processing. We compare the curves from Figs. 6–8. Curves 1 correspond to the analytical solutions. Curves 2, 3 and 4 correspond to the linear elements with reduced dispersion (the non-diagonal mass matrix) with 101, 201 and 251 dof, respectively. Curves 5 and 6 correspond to the isogeometric quadratic and 3rd-order elements with 101 dof.

linear elements with reduced dispersion require less computation time compared with the quadratic elements with reduced dispersion as explained above.

3.2. Space-discretization techniques with the diagonal mass matrix

In this section we will solve the 1-D impact problem using the spectral elements (up to the 10th-order) and the linear elements with reduced dispersion. For all these space-discretization methods, the diagonal mass matrices and the explicit central-difference method with very small time increments are used. As we mentioned before, the spectral 1st- and 2nd-order elements coincide with the standard finite elements of the same orders. Uniform meshes with 101 dof are used for all types of elements (except the spectral 3rd-order elements with 100 dof); see Figs. 13–17. In addition to these meshes, we also use uniform meshes with 201, 301 and 401 dof for the linear elements with reduced dispersion; see Fig. 19. Figs. 13–17 show the numerical solutions

for the velocity at different observation times. As can be seen, qualitatively the results for the spectral low- and high-order elements with the diagonal mass matrix are similar to those for the standard elements with the non-diagonal mass matrix (see the previous Section 3.2). Similar results we observe for the elements with reduced dispersion used with the non-diagonal (Fig. 8) and diagonal (Fig. 18) mass matrices. Fig. 19a,b shows that at the same number 101 of dof, the increase in the order of the spectral elements improves the accuracy; see curves 3–7. At the same number of dof, the linear elements with reduced dispersion are slightly more accurate than the standard 2nd-order elements with the lumped mass matrix; see curves 2 and 4 in Fig. 19a,b. Fig. 19c,d also shows that the linear elements with reduced dispersion and 201 dof are more accurate than the spectral 5th-order elements with 101 dof at time $T=18$ and are slightly less accurate than the spectral 5th-order elements with 101 dof at the large observation time $T=194$; see curves 2 and 6. Similarly, the linear elements with reduced dispersion and 301 dof are more accurate than the

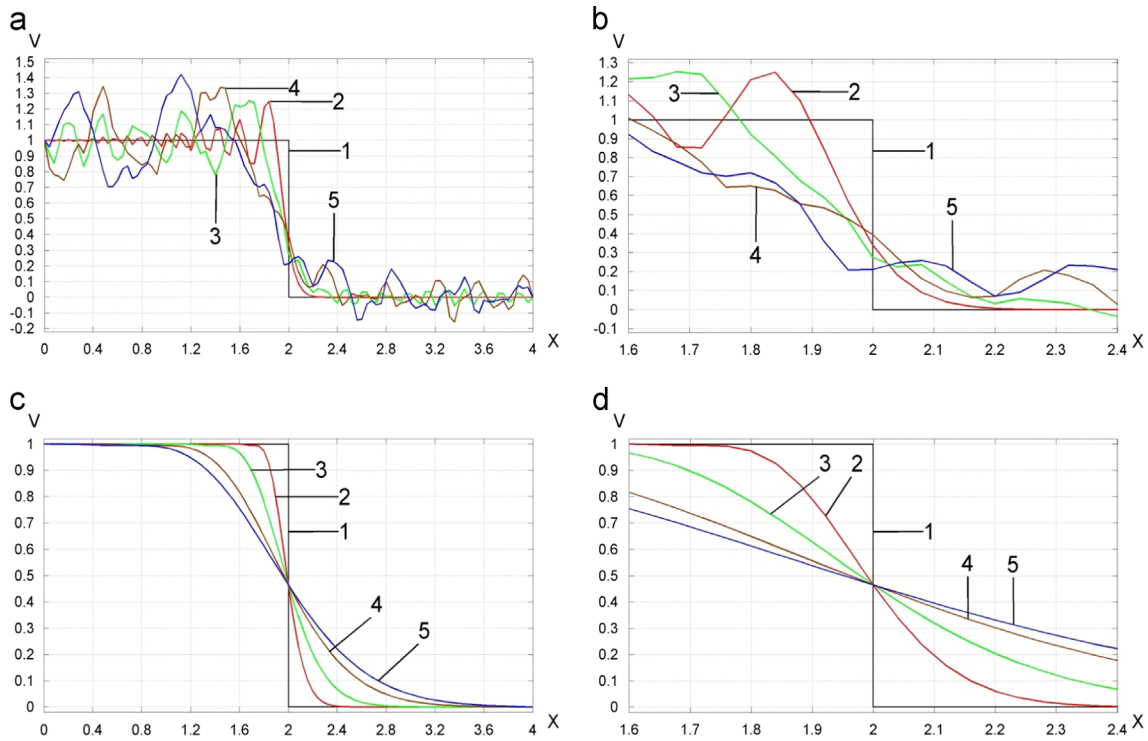


Fig. 13. The velocity distribution along the bar after (a, b) basic computations (the lumped mass matrix and small time increments) and after (c, d) post-processing. A uniform mesh with the standard (spectral) linear elements and 101 dof is used. Curves 1 correspond to the analytical solutions. Curves 2, 3, 4 and 5 correspond to the observation times $T = 2, 18, 98$ and 194 , respectively. (b) and (d) show the zoomed graphs (a) and (c) in the range $1.6 < x < 2.4$.

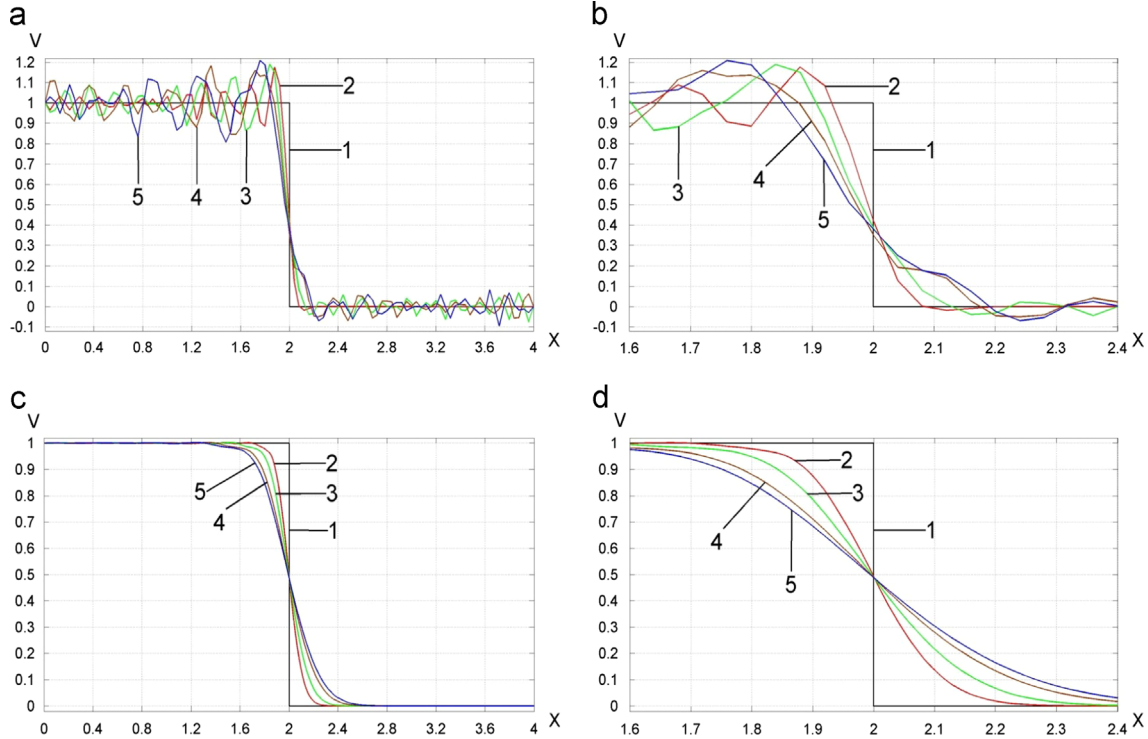


Fig. 14. The velocity distribution along the bar after (a, b) basic computations (the lumped mass matrix and small time increments) and after (c, d) post-processing. A uniform mesh with the standard (spectral) quadratic elements and 101 dof is used. Curves 1 correspond to the analytical solutions. Curves 2, 3, 4 and 5 correspond to the observation times $T = 2, 18, 98$ and 194 , respectively. (b) and (d) show the zoomed graphs (a) and (c) in the range $1.6 < x < 2.4$.

spectral 10th-order elements with 101 dof at time $T=18$ and yield practically the same accuracy as the spectral 10th-order elements with 101 dof at the large observation time $T=194$; see curves 3 and 7.

For the explicit time integration, the computations are often implemented on the level of elements without the calculation of the global mass and stiffness matrices. Therefore, the computation cost in this case is related to the multiplication of the local

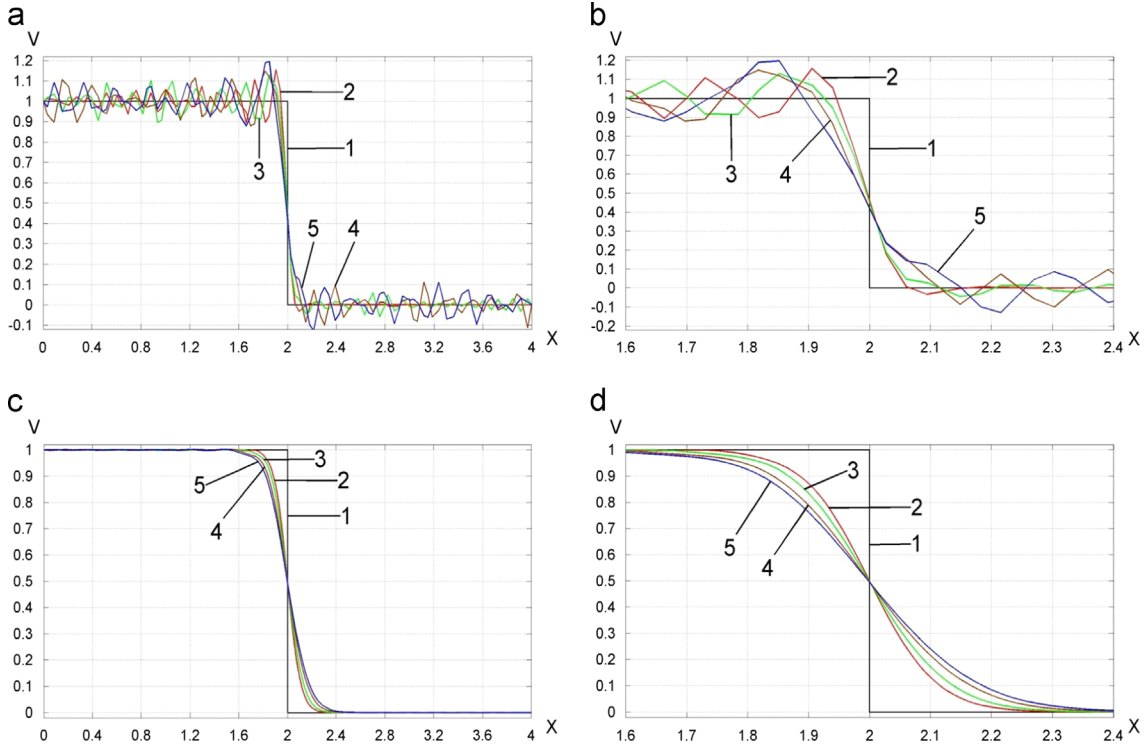


Fig. 15. The velocity distribution along the bar after (a, b) basic computations (the lumped mass matrix and small time increments) and after (c, d) post-processing. A uniform mesh with the spectral 3rd-order elements and 100 dof is used. Curves 1 correspond to the analytical solutions. Curves 2, 3, 4 and 5 correspond to the observation times $T = 2, 18, 98$ and 194 , respectively. (b) and (d) show the zoomed graphs (a) and (c) in the range $1.6 < x < 2.4$.

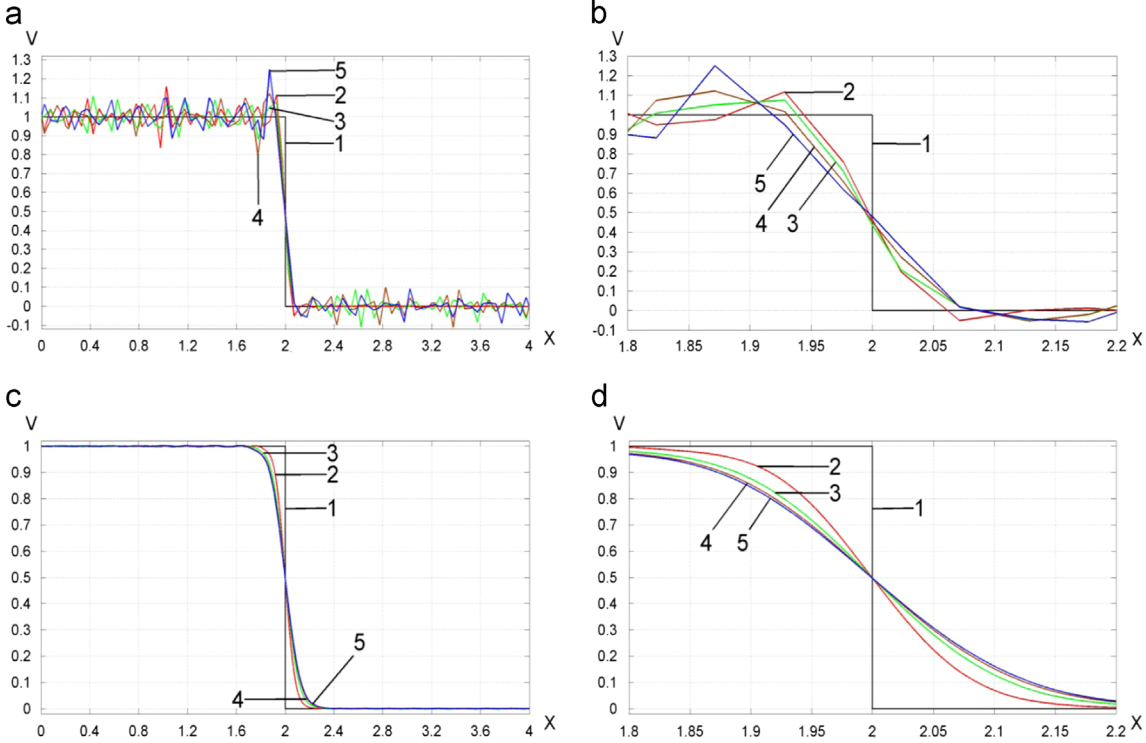


Fig. 16. The velocity distribution along the bar after (a, b) basic computations (the lumped mass matrix and small time increments) and after (c, d) post-processing. A uniform mesh with the spectral 5th-order elements and 101 dof is used. Curves 1 correspond to the analytical solutions. Curves 2, 3, 4 and 5 correspond to the observation times $T = 2, 18, 98$ and 194 , respectively. (b) and (d) show the zoomed graphs (a) and (c) in the range $1.8 < x < 2.2$.

effective stiffness matrix by a non-zero vector and is proportional to $n_{dof}^2 n_{el}$ where n_{dof} is the number of dof of one element and n_{el} is the number of elements. For example, $n_{dof}^2 n_{el} = 11^2 \times 10 = 1210$ for the spectral 10th-order elements with 101 dof and

$n_{dof}^2 n_{el} = 2^2 \times 300 = 1200$ for the linear elements with reduced dispersion and 301 dof; i.e., the computational costs are approximately the same in this case. However, we can reduce the computational cost for the linear elements with reduced dispersion by

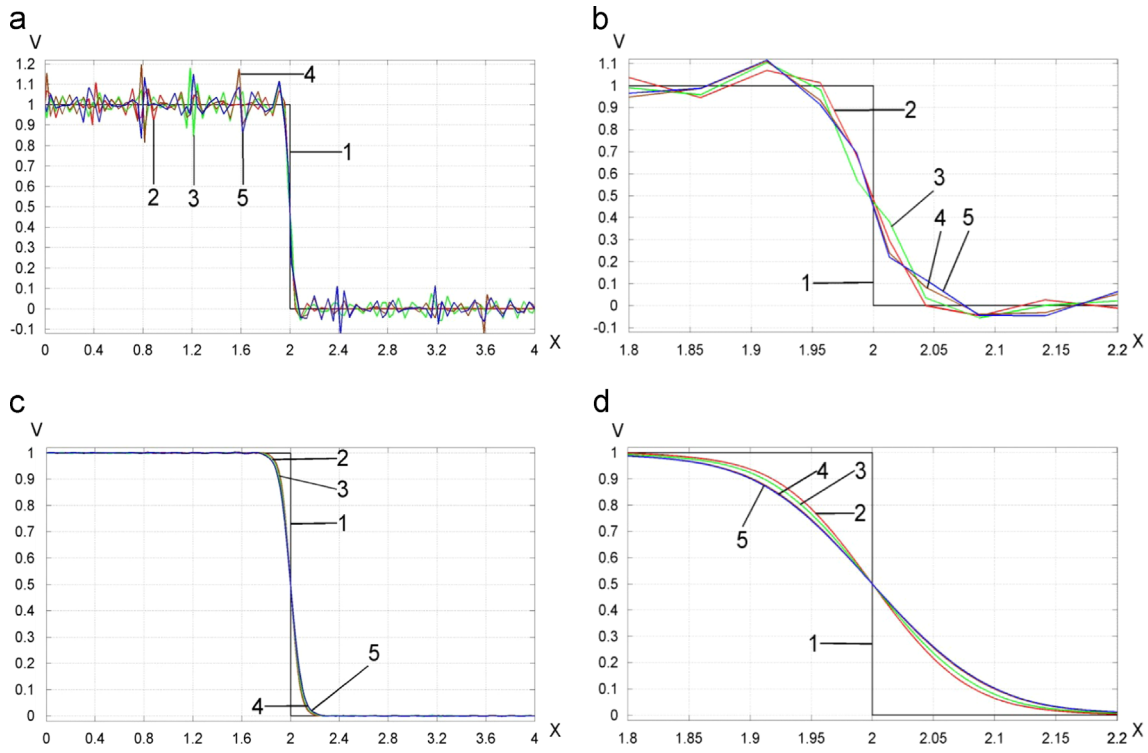


Fig. 17. The velocity distribution along the bar after (a, b) basic computations (the lumped mass matrix and small time increments) and after (c, d) post-processing. A uniform mesh with the spectral 10th-order elements and 101 dof is used. Curves 1 correspond to the analytical solutions. Curves 2, 3, 4 and 5 correspond to the observation times $T = 2, 18, 98$ and 194 , respectively. (b) and (d) show the zoomed graphs (a) and (c) in the range $1.8 < x < 2.2$.

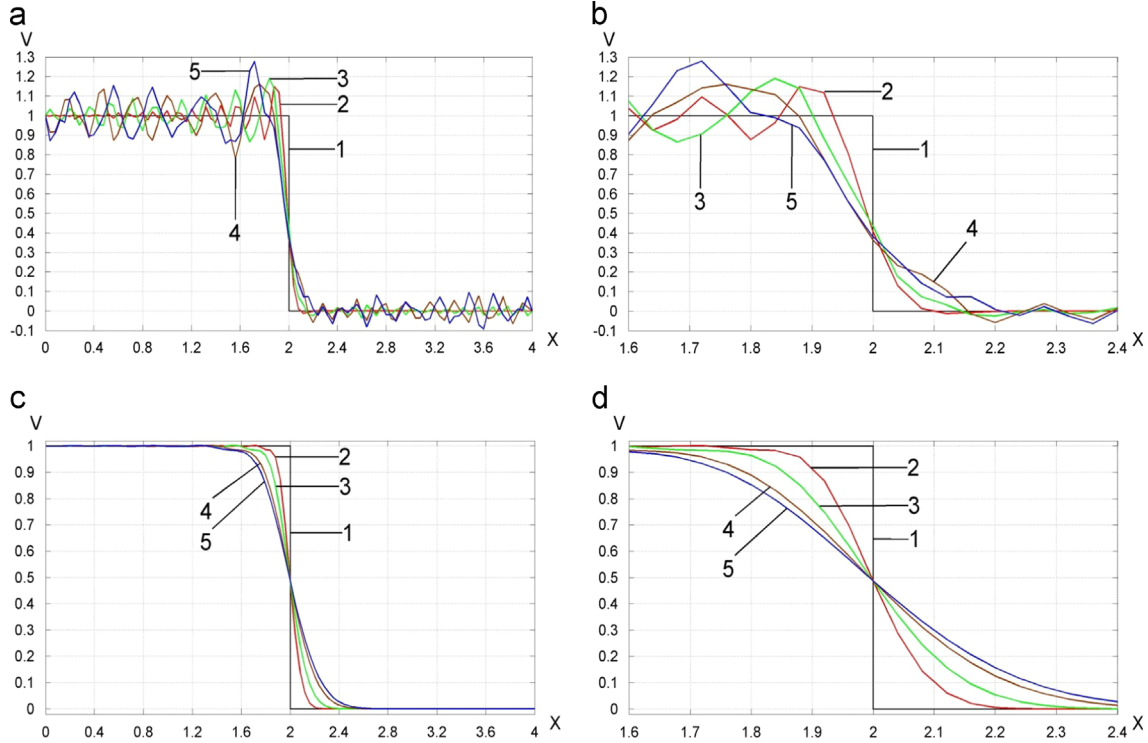


Fig. 18. The velocity distribution along the bar after (a, b) basic computations (the lumped mass matrix and small time increments) and after (c, d) post-processing. A uniform mesh with the linear elements with reduced dispersion and 101 dof is used. Curves 1 correspond to the analytical solutions. Curves 2, 3, 4 and 5 correspond to the observation times $T = 2, 18, 98$ and 194 , respectively. (b) and (d) show the zoomed graphs (a) and (c) in the range $1.6 < x < 2.4$.

the use of the following procedure. Let us combine every 30 linear elements (e.g., starting from the left end of the bar) into one superelement. In this case we will obtain $n_{el} = 10$ superelements.

The computation cost for $n_{el} = 10$ superelements is $n_{dof}bn_{el} = 31 \times 3 \times 10 = 930$ where $n_{dof} = 31$ is the number of dof of one superelement and $b=3$ is the bandwidth of the effective stiffness matrix

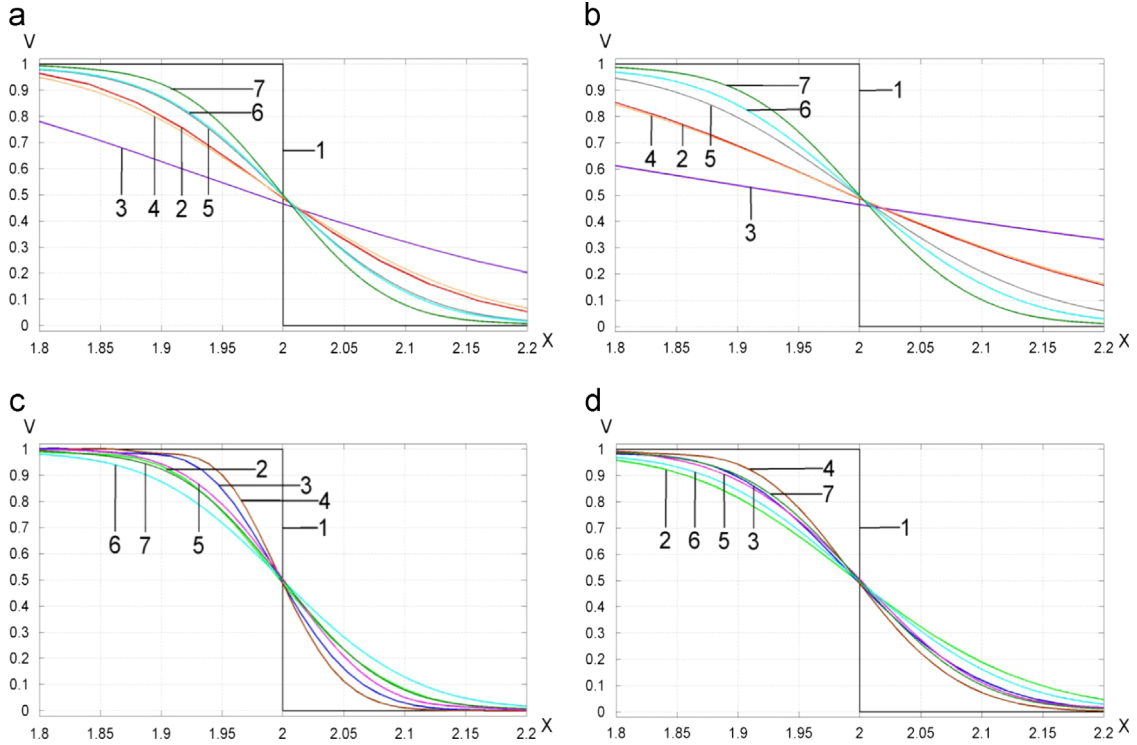


Fig. 19. The velocity distribution along the bar in the range $1.8 < x < 2.2$ at the observation times $T=18$ (a, c) and $T=194$ (b, d) after post-processing. We compare the curves from Figs. 7, 13, 14, 16, 17 and 18. Curves 1 correspond to the analytical solutions. Curves 2 in (a, b), 2 in (c, d), 3 in (c, d) and 4 in (c, d) correspond to the linear elements with reduced dispersion (the lumped mass matrix) with 101, 201, 301 and 401 dof, respectively. Curves 3 in (a, b), 4 in (a, b), 5 in (a, b), 6 and 7 correspond to the spectral linear, quadratic, 4th-order, 5th-order and 10th-order elements with 101 dof. Curves 5 in (c, d) correspond to the isogeometric 3rd-order elements with 101 dof.

of one superelement consisting of 30 linear elements with reduced dispersion. This means that at the same or better accuracy (e.g., see curves 3 and 7 in Fig. 19c,d at the observation times $T=18$ and $T=194$), the linear elements with reduced dispersion and 301 dof require less computation time and are more computationally efficient compared with the spectral 10th-order elements with 101 dof at times $T=18$ and $T=194$.

In order to compare the accuracy of the numerical results obtained with the different space-discretization techniques as well as with the implicit and explicit time-integration methods, Fig. 19c,d also includes the numerical solutions obtained by the isogeometric 3rd-order elements (the non-diagonal mass matrix) with 101 dof. As can be seen, the accuracy of the isogeometric 3rd-order elements at time $T=18$ and $T=194$ is close to that of the spectral 10th-order elements at the same number of dof; see curves 5 and 7.

It is interesting to note that the size of time increments at the filtering stage calculated according to the formulas Eqs. (A.1) and (A.2) from the Appendix indirectly defines the range of actual frequencies included into the numerical solutions after the filtering stage (because spurious high-frequencies are damped out at the filtering stage) and can be used for the comparison of the accuracy of different space-discretization techniques; see our papers [4,42,44]. If at the selected observation time T the time increment at the filtering stage for one space-discretization technique is smaller than that for another space-discretization technique then the former technique yields more accurate results at time T than the latter technique (if time increments are close to each other then the techniques include the same ranges of actual frequencies and yield approximately the same results). This is similar to the modal decomposition method for which the increase in the range of actual frequencies leads to the increase in the accuracy of numerical results. This also means that Eqs. (A.1) and (A.2) allow the quantitative comparison of the accuracy of

different space-discretization techniques. For example, according to Eqs. (A.1) and (A.2), we use the following time increments for the filtering stage at time $T=18$: $\Delta t_1 = 0.0405$, $\Delta t_2 = 0.0235$, $\Delta t_3 = 0.0171$ and $\Delta t_4 = 0.0137$ for the linear elements with reduced dispersion (the diagonal mass matrix) with 101 dof, 201 dof, 301 dof and 401 dof, respectively; $\Delta t_5 = 0.0448$ for the standard quadratic elements (the diagonal mass matrix) with 101 dof; $\Delta t_6 = 0.0222$ for the spectral 10th-order elements (the diagonal mass matrix) with 101 dof; $\Delta t_7 = 0.0188$ for the isogeometric 3rd-order elements (the consistent mass matrix) with 101 dof. At the large observation time $T=194$, we have the following time increments for the filtering stage: $\Delta t_1 = 0.0679$, $\Delta t_2 = 0.0395$, $\Delta t_3 = 0.0288$ and $\Delta t_4 = 0.0230$ for the linear elements with reduced dispersion (the diagonal mass matrix) with 101 dof, 201 dof, 301 dof and 401 dof, respectively; $\Delta t_5 = 0.0695$ for the standard quadratic elements (the diagonal mass matrix) with 101 dof; $\Delta t_6 = 0.0266$ for the spectral 10th-order elements (the diagonal mass matrix) with 101 dof; $\Delta t_7 = 0.0269$ for the isogeometric 3rd-order elements (the consistent mass matrix) with 101 dof. Comparing these time increments at the same observation time, we can compare the accuracy of the numerical results discussed above. For example, at times $T=18$ and $T=194$, the time increments Δt_6 and Δt_7 are close to each other and the corresponding space-discretization techniques yield approximately the same accuracy; see curves 5 and 7 in Fig. 19c,d (similar results we have for the time increments Δt_1 and Δt_5 ; see curves 2 and 4 in Fig. 19a,b). We also have that $\Delta t_3 < \Delta t_6$ at time $T=18$ and $\Delta t_3 > \Delta t_6$ at time $T=194$ (see curves 3 and 7 in Fig. 19c,d and the comparison of the spectral elements and the linear elements with reduced dispersion described above in this section). It can be also seen that Δt_4 has the smallest value among all presented time increments and the corresponding linear elements with reduced dispersion and 401 dof yield the most accurate results; see curves 4 in Fig. 19c,d.

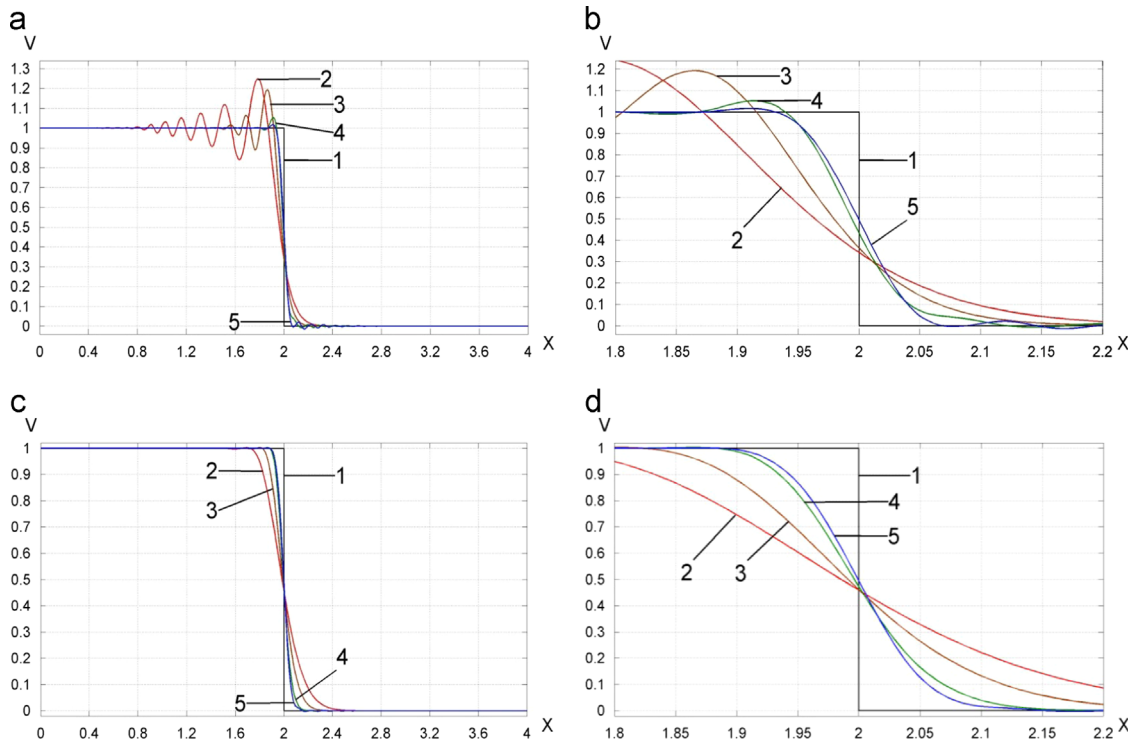


Fig. 20. The velocity distribution along the bar at the observation time $T=2$ after (a, b) basic computations (the consistent mass matrix and small time increments) and after (c, d) post-processing. A uniform mesh with the isogeometric 3rd-order elements and 101 dof is used. Curves 2, 3, 4 and 5 correspond to the following time increments in basic computations: $d\bar{t}$, $0.5d\bar{t}$, $0.2d\bar{t}$ and $0.1d\bar{t}$, respectively ($d\bar{t}=0.04$). (b) and (d) show the zoomed graphs (a) and (c) in the range $1.8 < x < 2.2$.

3.3. The effect of the size of time increments in basic computations on the accuracy of numerical results obtained by different space-discretization techniques

In this section we will analyze the effect of a time increment in basic computations on the accuracy of the numerical results obtained by the isogeometric elements (used with the implicit time-integration method) and by the spectral high-order elements (used with the explicit time-integration method). We will show that very small time increments for these techniques yield more accurate results. Uniform meshes with 101 dof are used. Because implicit time-integration methods can be used with any size of time increments, then we will use $d\bar{t}=0.04$ as the largest time increment for the isogeometric elements. This time increment $d\bar{t}=0.04$ corresponds to the stability limit of the standard linear finite elements with the lumped mass matrix at the same number 101 of dof. For the spectral high-order elements with the lumped mass matrix we estimate the stability limit dt^{st} from numerical experiments and then use the time increments that are close and smaller than the stability limit. Figs. 20–28 show the effect of time increments on the accuracy of numerical results for the isogeometric 3rd-order elements as well for the spectral 3rd- and 10th-order elements. As can be seen, the results significantly depend on the observation time and the size of time increments in basic computations. In all cases, the decrease in the size of time increments in basic computations leads to the increase in the accuracy. We should also note that for the same elements, smaller time increments should be used at a larger observation time in order to get accurate results. However, in order to decrease the computation cost, the size of time increments should be as large as possible. As can be seen from Fig. 20, for the isogeometric 3rd-order elements at time $T=2$, time increments $0.2d\bar{t}$ yield accurate results (the further time refinement does not significantly increase the accuracy). However, for the same elements, much smaller time increments $0.1d\bar{t}$ and $0.03d\bar{t}$ can be recommended at times $T=18$

and $T=194$; respectively (see Figs. 21 and 22). Qualitatively, similar results are obtained for the spectral 3rd- and 10th-order elements in Figs. 23–28. For example, for the short observation time $T=2$ accurate numerical results for these elements can be obtained at time increments $0.95dt^{st}$ which are close to the stability limit ($dt^{st}=0.02817$ and $dt^{st}=0.01130$ for the spectral 3rd-order and 10th-order elements, respectively); see Figs. 23 and 26. However, for larger observation times, the time increments should be significantly decreased; e.g., $0.1dt^{st}$ at the large observation time $T=194$ (see Figs. 25 and 28). The results presented here show that small time increments in basic computations that yield a very small error in time should be used. In our paper [47] we have derived an exact, closed-form a-priori global error estimator for 2nd-order time-integration methods and have shown that in order to have the same error in time at different observation times for each mode, the following relationships between time increments dt_1 and dt_2 used at different observation times T_1 and T_2 should be met $dt_1/dt_2 = \sqrt{T_2/T_1}$. This error estimator is in a good agreement with the numerical results obtained above and can be used as follows. At a short observation time T_1 , the appropriate size dt_1 of time increments can be found from numerical experiments (e.g. using the time refinement). Then, for a large observation time T_2 , the size of time increments can be found with the formula $dt_2 = dt_1 \sqrt{T_1/T_2}$ for the 2nd-order time-integration methods (similar formulas have been also derived for high-order time-integration methods; see our papers [42,47]).

Remark 1. For more accurate space-discretization techniques (e.g., the isogeometric 3rd-order elements or the spectral 10th-order elements) higher-frequencies are resolved more accurately compared with less accurate space-discretization techniques. It is also known that during time integration, at the same time increments the error in time is greater for higher modes. Therefore, more accurate space-discretization techniques require smaller time increments in order to have accurate results at higher modes.

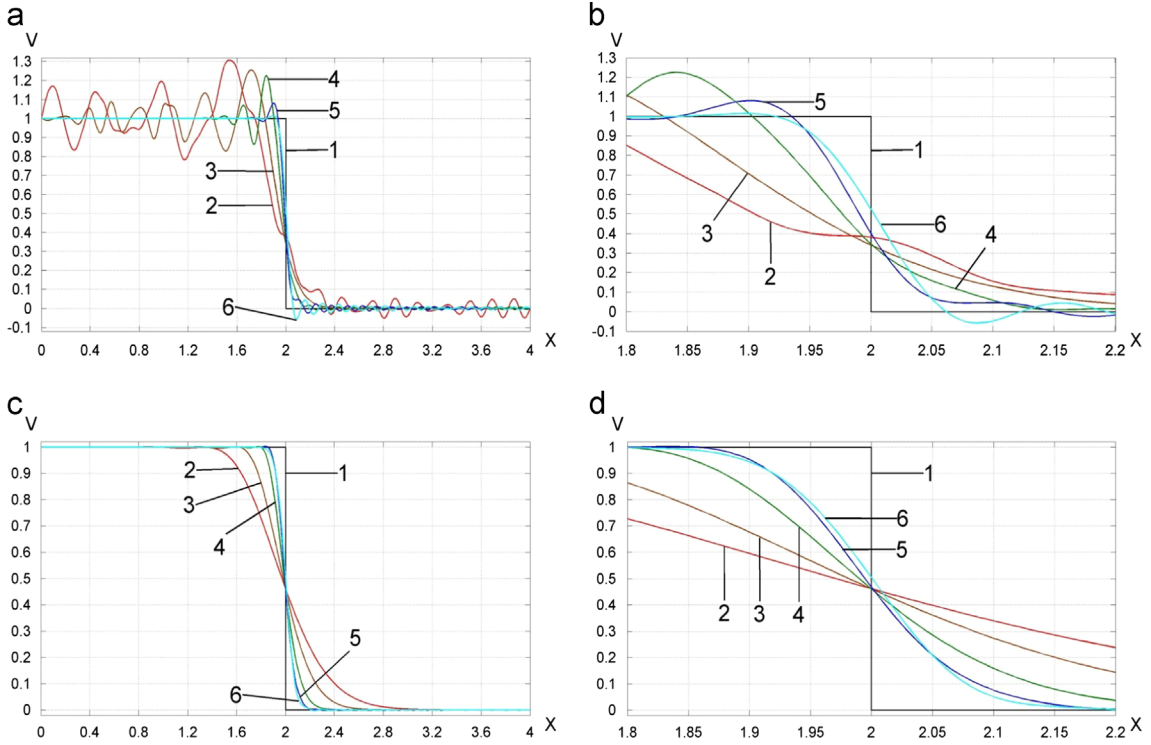


Fig. 21. The velocity distribution along the bar at the observation time $T=18$ after (a, b) basic computations (the consistent mass matrix and small time increments) and after (c, d) post-processing. A uniform mesh with the isogeometric 3rd-order elements and 101 dof are used. Curves 2, 3, 4, 5 and 6 correspond to the following time increments in basic computations: $d\bar{\tau}$, $0.5d\bar{\tau}$, $0.2d\bar{\tau}$, $0.1d\bar{\tau}$ and $0.01d\bar{\tau}$, respectively ($d\bar{\tau}=0.04$). (b) and (d) show the zoomed graphs (a) and (c) in the range $1.8 < x < 2.2$.

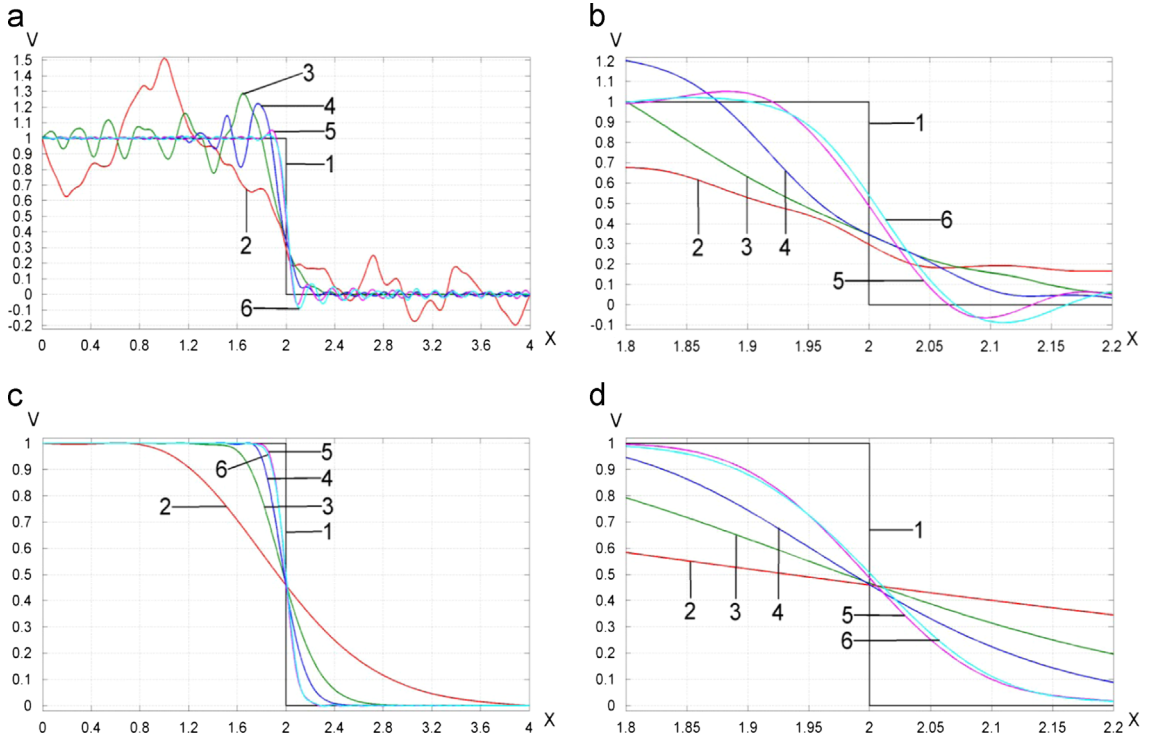


Fig. 22. The velocity distribution along the bar at the observation time $T=194$ after (a, b) basic computations (the consistent mass matrix and small time increments) and after (c, d) post-processing. A uniform mesh with the isogeometric 3rd-order elements and 101 dof are used. Curves 2, 3, 4, 5 and 6 correspond to the following time increments in basic computations: $d\bar{\tau}$, $0.2d\bar{\tau}$, $0.1d\bar{\tau}$, $0.03d\bar{\tau}$ and $0.01d\bar{\tau}$, respectively ($d\bar{\tau}=0.04$). (b) and (d) show the zoomed graphs (a) and (c) in the range $1.8 < x < 2.2$.

Remark 2. Except the 1-D case with the standard linear finite elements and the lumped mass matrix as well as the linear finite elements with reduced dispersion and the lumped mass matrix

(which are equivalent at the time increments equal to the stability limit; see our paper [4]), the decrease in the size of time increments in basic computations improves the accuracy of

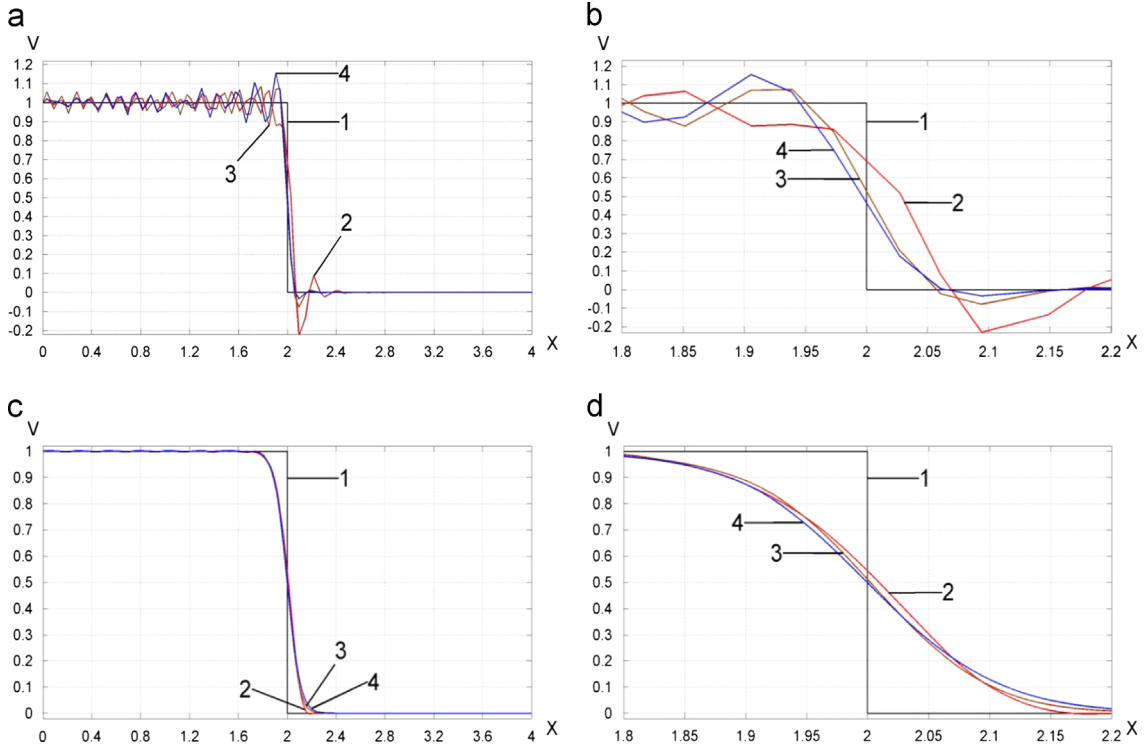


Fig. 23. The velocity distribution along the bar at the observation time $T=2$ after (a, b) basic computations (the lumped mass matrix and small time increments) and after (c, d) post-processing. A uniform mesh with the spectral 3rd-order elements and 100 dof is used. Curves 2, 3 and 4 correspond to the following time increments in basic computations: $0.95dt^{st}$, $0.5dt^{st}$ and $0.1dt^{st}$, respectively ($dt^{st}=0.02817$). (b) and (d) show the zoomed graphs (a) and (c) in the range $1.8 < x < 2.2$.

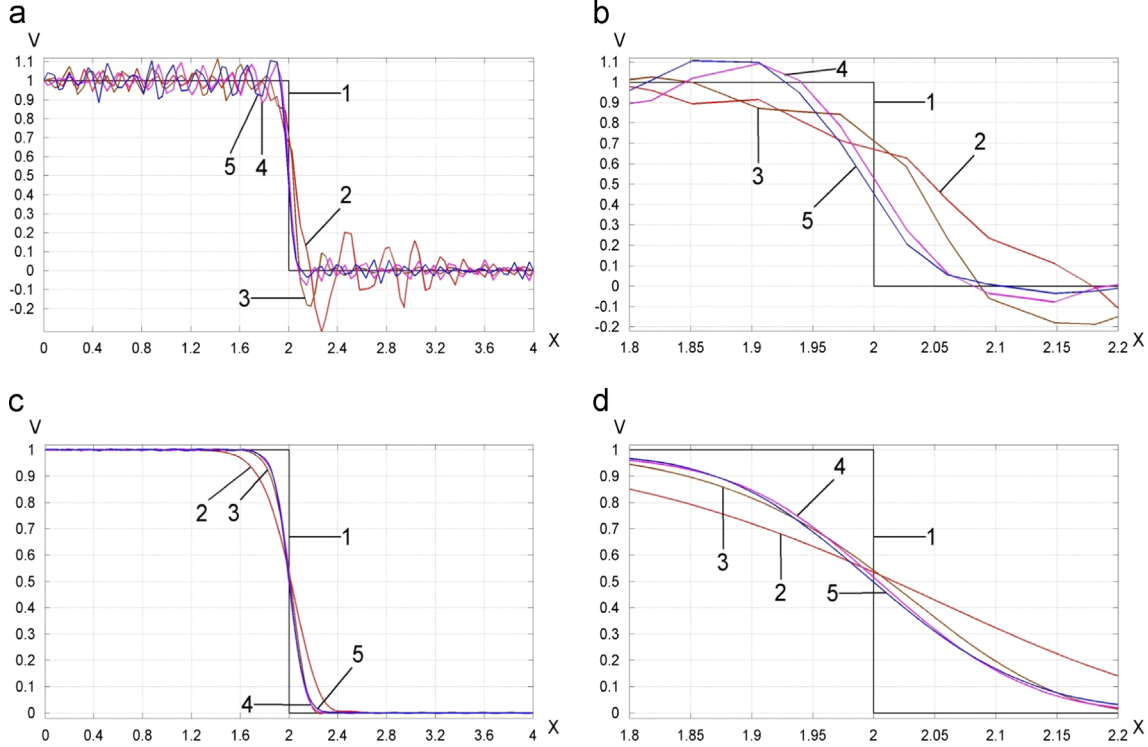


Fig. 24. The velocity distribution along the bar at the observation time $T=18$ after (a, b) basic computations (the lumped mass matrix and small time increments) and after (c, d) post-processing. A uniform mesh with the spectral 3rd-order elements and 100 dof is used. Curves 2, 3, 4 and 5 correspond to the following time increments in basic computations: $0.95dt^{st}$, $0.5dt^{st}$, $0.3dt^{st}$ and $0.1dt^{st}$, respectively ($dt^{st}=0.02817$). (b) and (d) show the zoomed graphs (a) and (c) in the range $1.8 < x < 2.2$.

numerical results for all other space-discretization techniques considered in the paper. In the 2-D and 3-D cases, the standard linear finite elements with the lumped mass matrix and the linear

finite elements with reduced dispersion and the lumped mass matrix yield accurate results at small time increments (e.g., see our paper [4]). Therefore, we analyze and compare these elements in

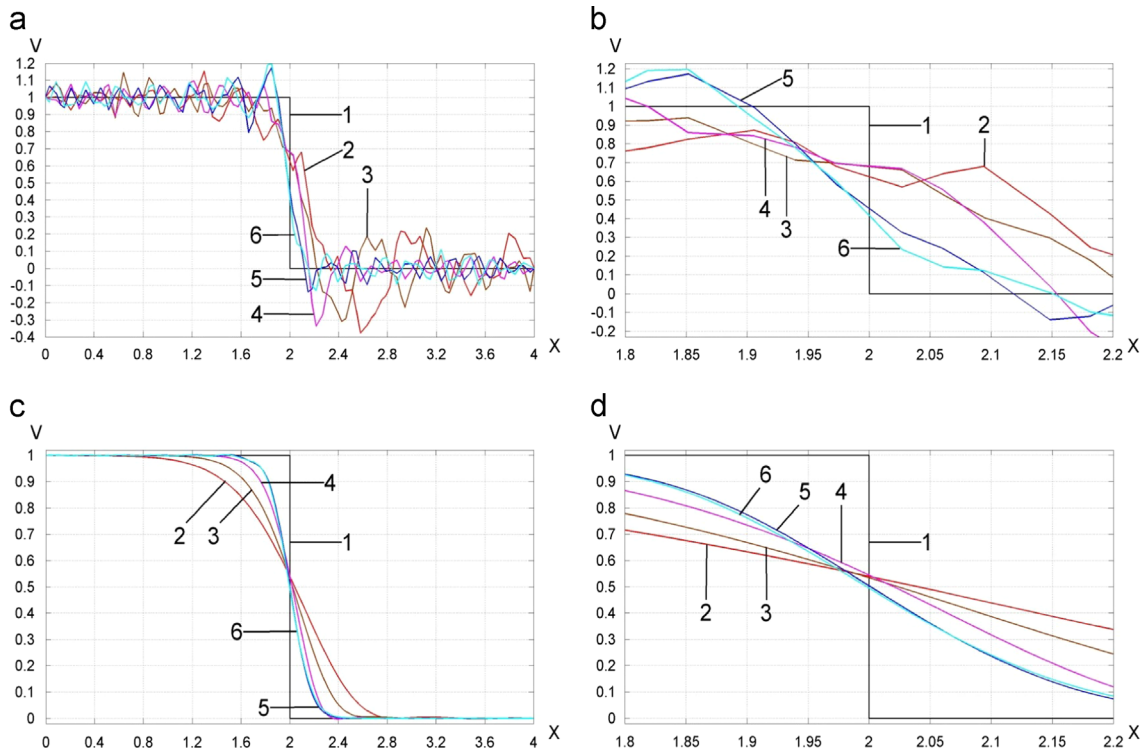


Fig. 25. The velocity distribution along the bar at the observation time $T=194$ after (a, b) basic computations (the lumped mass matrix and small time increments) and after (c, d) post-processing. A uniform mesh with the spectral 3rd-order elements and 100 dof is used. Curves 2, 3, 4, 5 and 6 correspond to the following time increments in basic computations: $0.95dt^{st}$, $0.5dt^{st}$, $0.3dt^{st}$, $0.1dt^{st}$ and $0.01dt^{st}$, respectively ($dt^{st}=0.02817$). (b) and (d) show the zoomed graphs (a) and (c) in the range $1.8 < x < 2.2$.

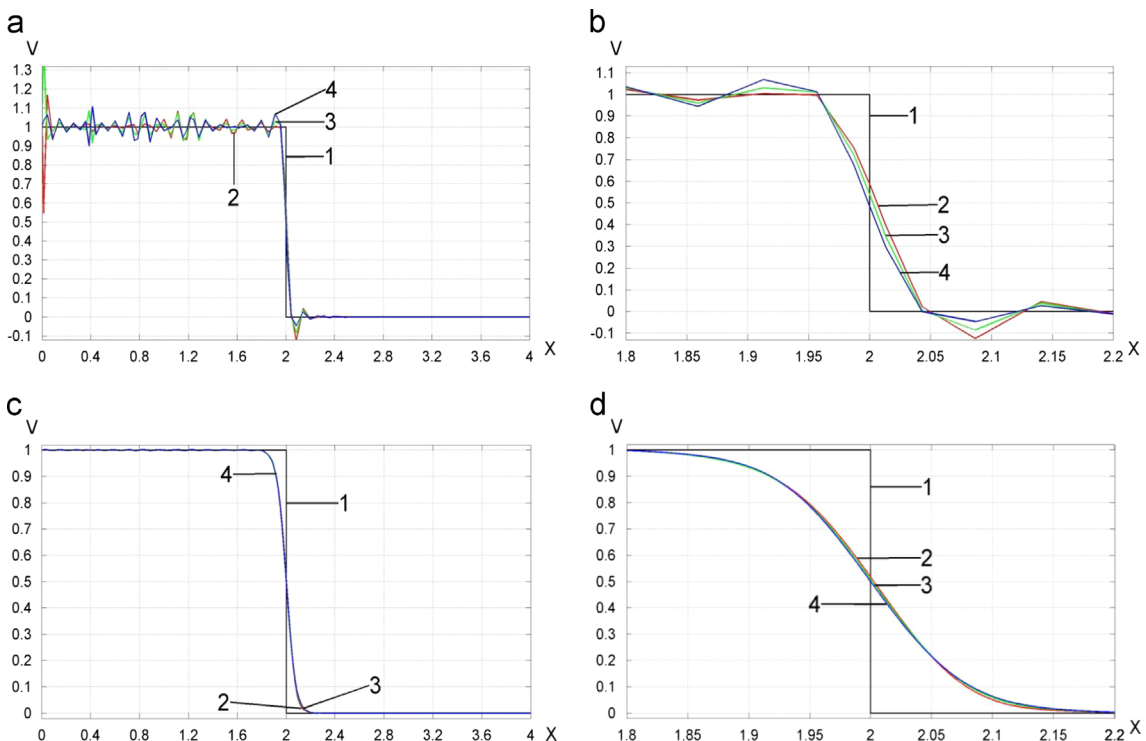


Fig. 26. The velocity distribution along the bar at the observation time $T=2$ after (a, b) basic computations (the lumped mass matrix and small time increments) and after (c, d) post-processing. A uniform mesh with the spectral 10th-order elements and 100 dof is used. Curves 2, 3 and 4 correspond to the following time increments in basic computations: $0.95dt^{st}$, $0.7dt^{st}$ and $0.1dt^{st}$, respectively ($dt^{st}=0.0113$). (b) show the zoomed graphs (a) in the range $1.8 < x < 2.2$. (d) show the zoomed graphs (c) in the range $1.8 < x < 2.2$.

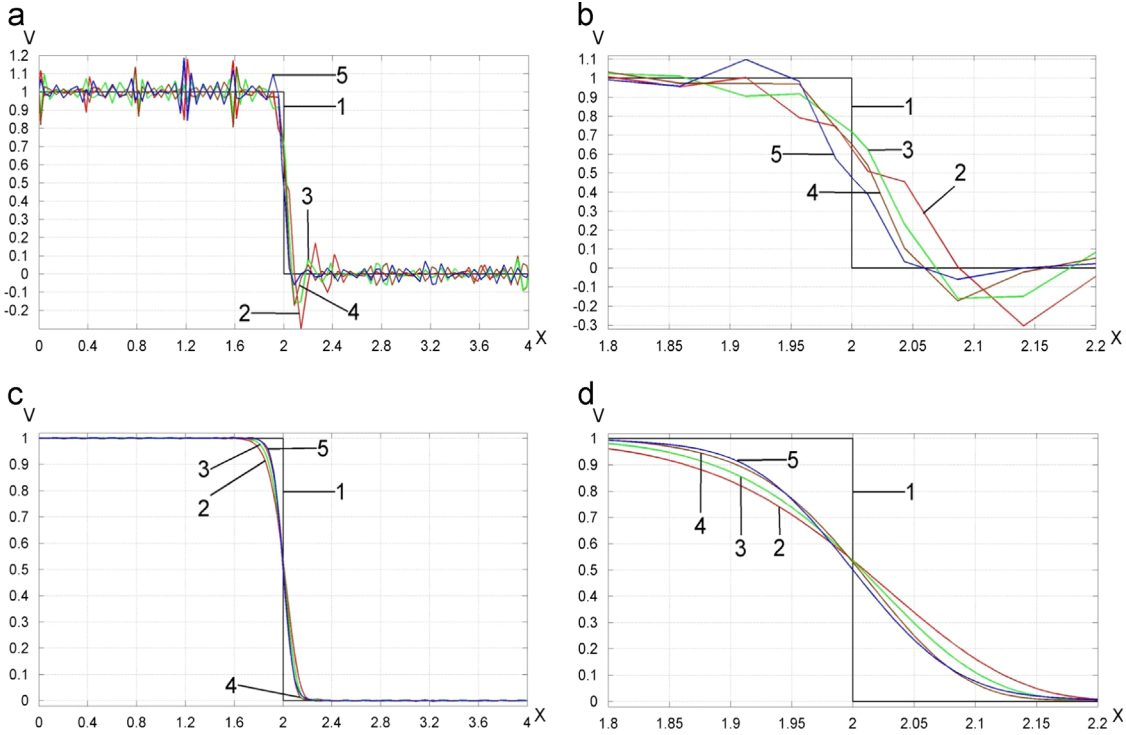


Fig. 27. The velocity distribution along the bar at the observation time $T=18$ after (a, b) basic computations (the lumped mass matrix and small time increments) and after (c, d) post-processing. A uniform mesh with the spectral 10th-order elements and 101 dof is used. Curves 2, 3, 4 and 5 correspond to the following time increments in basic computations: $0.95dt^{st}$, $0.7dt^{st}$, $0.5dt^{st}$ and $0.1dt^{st}$, respectively ($dt^{st}=0.0113$). (b) and (d) show the zoomed graphs (a) and (c) in the range $1.8 < x < 2.2$.

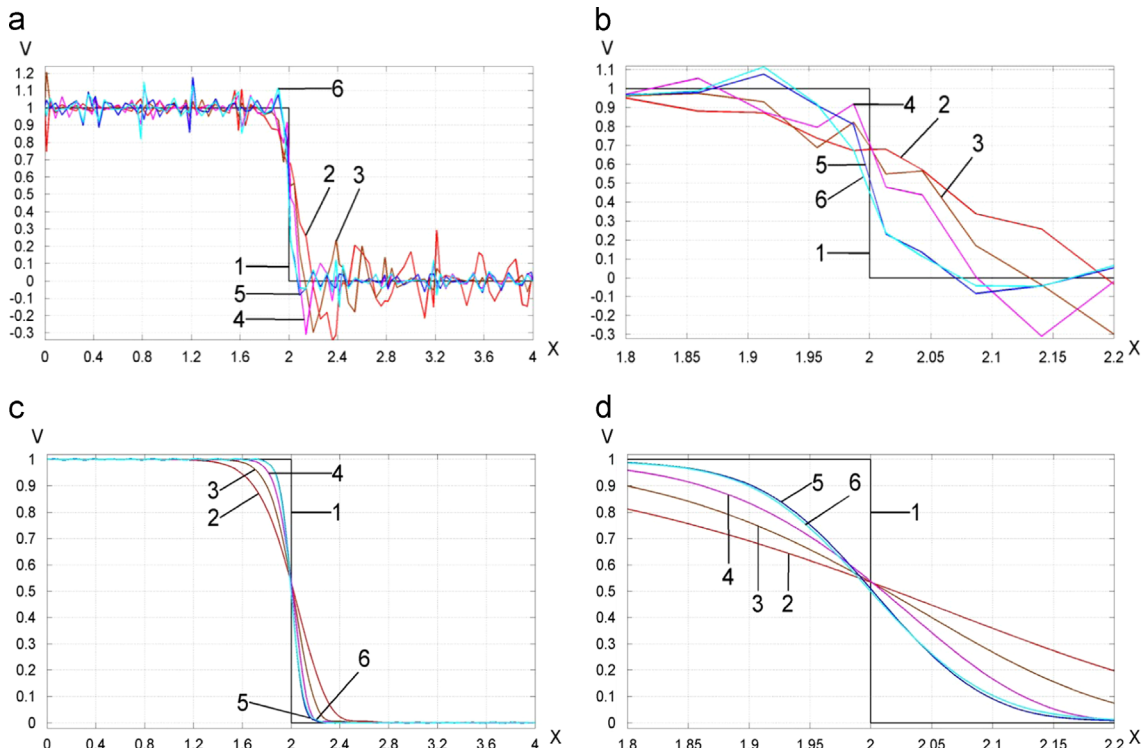


Fig. 28. The velocity distribution along the bar at the observation time $T=194$ after (a, b) basic computations (the lumped mass matrix and small time increments) and after (c, d) post-processing. A uniform mesh with the spectral 10th-order elements and 101 dof is used. Curves 2, 3, 4, 5 and 6 correspond to the following time increments in basic computations: $0.95dt^{st}$, $0.5dt^{st}$, $0.3dt^{st}$, $0.1dt^{st}$, and $0.01dt^{st}$, respectively ($dt^{st}=0.0113$). (b) and (d) show the zoomed graphs (a) and (c) in the range $1.8 < x < 2.2$.

Section 3.2 at small time increments in order to predict their accuracy in the multi-dimensional cases.

4. A 2-D transient acoustic problem with impact loading

Here, we will consider the solution of a 2-D transient acoustic problem described by the scalar wave equation

$$\frac{\partial^2 u}{\partial t^2} - c_o^2 \nabla^2 u = 0, \quad (7)$$

where u is the field variable, c_o is the wave velocity. The application of the space discretization to Eq. (7) leads to the semi-discrete system, Eq. (1). In this section we will show that the two-stage time integration technique yields accurate numerical results for acoustic wave propagation obtained by different space-discretization techniques in the multidimensional case. Similar to the 1-D case, the size of time increments at the filtering stage for multidimensional problems (see Eq. (A.3) in the Appendix for acoustic problems and our papers [5,42] for elastodynamics problems) indirectly defines the border between the actual frequencies and the spurious high frequencies; i.e., indirectly defines the ranges of actual and spurious frequencies in the multidimensional case. Therefore, it can be used for the comparison and the prediction of accuracy of numerical results obtained by different space-discretization techniques. Because currently we do not have computer codes for all space-discretization techniques in the multidimensional case, here we will show 2-D examples of the application of the two-stage time integration technique to the standard linear and quadratic finite elements as well as to the linear elements with reduced dispersion used with non-diagonal mass matrices.

Remark. A detailed study of the dispersion error for the linear elements with reduced dispersion applied to the 2-D acoustics problems is also presented in our paper [48] with the corresponding numerical examples.

Let us consider a square plate of length 1×1 , see Fig. 29a. The wave velocity is chosen to be $c_o=1$. The following boundary conditions are applied: $\partial u / \partial n = 0$ along the boundary AB , EC , CD and AD ($\partial / \partial n$ is the normal derivative at the boundary); along the part BE of the upper boundary, an impact loading is prescribed in terms of the value of the field variable $u_{BE} = t$ (this corresponds to the instantaneous application of the velocity $v_{BE} = 1$). Zero initial conditions are used; i.e., $u(x, y, 0) = v(x, y, 0) = 0$. The observation time is chosen to be $T = 1.5$. During this time the waves travel from the boundary BE to all other boundaries, reflect from them and produce a complicated distribution of the velocity field at time $T = 1.5$, e.g., see Fig. 29b,c.

The problem is solved on uniform meshes with $100 \times 100 = 10,000$ and $300 \times 300 = 90,000$ linear Q4 four-node quadrilateral finite elements and on uniform meshes with $50 \times 50 = 2500$ and $66 \times 66 = 4356$ quadratic Q9 nine-node quadrilateral finite elements. For the linear Q4 elements we use the standard approach with the consistent mass matrix as well as the formulation with reduced dispersion for which the mass and stiffness matrices are calculated using the modified integration rule; see [9] (in the 1-D case this technique coincides with the averaged mass matrix technique used in Section 3). For the quadratic Q9 elements we use the standard formulation with the consistent mass matrix. The trapezoidal rule with very small time increments is used in basic computations for all numerical results. The time increments at the filtering stage are calculated according to Eqs. (A.1)–(A.3) for the linear and quadratic finite elements with the corresponding coefficients a_1 and a_2 from Table 1. Because we do not know the exact solution to the problem under consideration, the numerical

solution after the filtering stage obtained on the fine mesh with $300 \times 300 = 90,000$ linear finite elements with reduced dispersion is considered as a reference solution (we should also mention that the numerical solutions after the filtering stage converge to the unique solution at mesh refinement).

The numerical solutions after the stage of basic computations include large spurious high-frequency oscillations even for the results obtained by the linear elements with reduced dispersion; see Fig. 29b. These oscillations are removed from the numerical results at the filtering stage, see Fig. 29c. The spurious oscillations can be better seen when we plot the velocity along the boundary AB ; see Fig. 30a–c. Due to these oscillations, the results obtained with the different space-discretization techniques are inaccurate and it is unclear how to compare them. However, after removing the spurious oscillations at the filtering stage, we can compare the numerical results (see curves 1–5 in Fig. 30d) with the reference solution (see curve 6 in Fig. 30d). As can be seen, at the same number of dof (for the meshes with $100 \times 100 = 10,000$ Q4 elements and with $50 \times 50 = 2500$ Q9 elements), the linear elements with reduced dispersion yield the most accurate results (see curve 1 in Fig. 30d). We can also see that the results obtained with the standard $300 \times 300 = 90,000$ Q4 elements, with the standard $66 \times 66 = 4356$ Q9 elements and with $100 \times 100 = 10,000$ Q4 elements with reduced dispersion are approximately the same. This means that at the same accuracy at $T = 1.5$, the linear elements with reduced dispersion reduce the number of dof by a factor of 9 compared with the standard Q4 elements and by a factor of 1.75 compared with the standard Q9 elements (moreover, the matrix bandwidth for Q9 elements is larger than the matrix bandwidth for Q4 elements and this leads to additional computational costs for Q9 elements). Similar to the 1-D case, the results of this comparison can be predicted by the size of time increments used at the filtering stage that indirectly defines the range of actual frequencies used in the numerical results. For example, according to Eqs. (A.1)–(A.3), the following time increments are used at the filtering stage: $\Delta t_1 = 0.00682$, $\Delta t_2 = 0.01442$, $\Delta t_3 = 0.00836$, $\Delta t_4 = 0.00683$, $\Delta t_5 = 0.00676$ for the meshes with $100 \times 100 = 10,000$ Q4 (reduced dispersion), $100 \times 100 = 10,000$ Q4 (standard), $50 \times 50 = 2500$ Q9 (standard), $300 \times 300 = 90,000$ Q4 (standard) and $66 \times 66 = 4356$ Q9 (standard) finite elements, respectively. As indicated in Section 3.2, a smaller size of time increments at the filtering stage corresponds to more accurate results; independent of space-discretization methods used, the same sizes of time increments at the filtering stage approximately correspond to the same accuracy; i.e., the sizes Δt_i ($i = 1, 2, \dots, 5$) predict the accuracy of the numerical results presented in Fig. 30d.

Remark. The examples of the application of the two-stage time-integration approach to the elastodynamics problems can be found in our papers [4,42,44] for some selected space-discretization techniques in the multidimensional case. Similar to Section 4, they show the validity of the results obtained in Section 3 for 2-D and 3-D elastodynamics problems.

5. Concluding remarks

One issue with numerical solutions of wave propagation problems by different space-discretization techniques is the presence of spurious high-frequency oscillations. The range of spurious high frequencies is different for different space-discretization methods. We have not seen in the literature the numerical approaches that quantify and filter out all spurious oscillations from numerical solutions even solved by the popular space-discretization techniques such as the standard, spectral and isogeometric high-order finite elements. We have resolved this issue

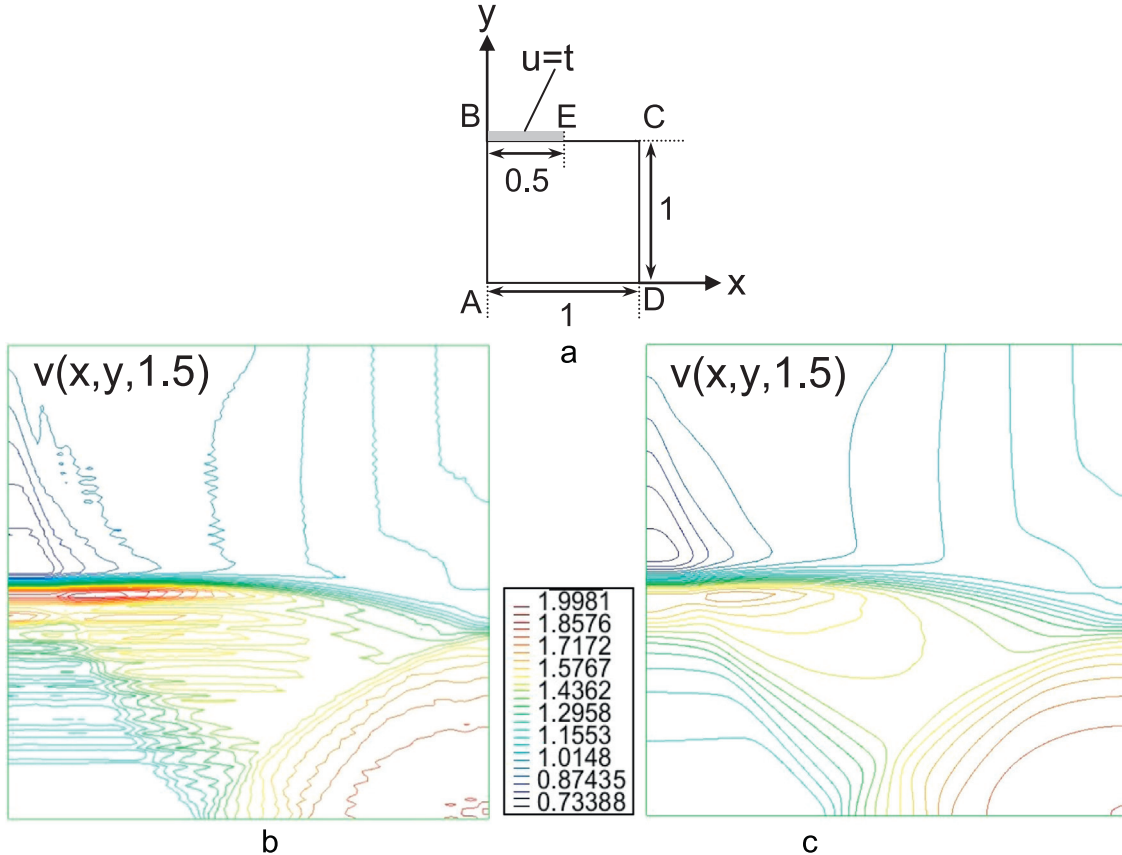


Fig. 29. A 2-D transient acoustic problem with impact loading (a). The distribution of the velocity $v(x,y,1.5)$ at the observation time $T=0.15$ after basic computations (b) and after the filtering stage (c). A uniform mesh with $100 \times 100 = 10,000$ linear Q4 finite elements with reduced-dispersion is used.

Table 1
Coefficients a_1 and a_2 for different space-discretization techniques.

Types of elements	Coefficients	Order of elements					
		1st	2nd	3rd	4th	5th	10th
Standard finite elements (consistent mass matrix)	a_1	0.3574	0.3156	0.4485	0.5495	0.5115	
	a_2	0.3204	0.2364	0.1571	0.1111	0.1078	
Spectral elements (lumped mass matrix)	a_1	0.3342	0.448	0.5659	0.4790	0.4461	0.4317
	a_2	0.3363	0.1845	0.1139	0.1128	0.1073	0.0759
Isogeometric elements (consistent mass matrix)	a_1		0.2513	0.2311			
	a_2		0.2035	0.1508			
Finite elements with reduced Dispersion (non-diagonal matrix)	a_1	0.2979	0.5595				
	a_2	0.2074	0.1097				
Linear elements with reduced Dispersion (diagonal matrix)	a_1	0.3296					
	a_2	0.2180					

by the application of the two-stage time-integration approach recently developed in our papers; e.g., see [5,41,42].

Another important result of the paper is related to the comparison of accuracy of different space-discretization techniques used for the solution of transient acoustics and elastodynamics problems. One way to compare the accuracy of these techniques is based on the evaluation of the numerical dispersion error. However, this error is related to a selected mode of the elastodynamics system and does not prescribe the combined effect of all modes on the accuracy. Moreover, the dispersion error does not estimate the effect of the observation time and time increments on the accuracy of numerical results. Therefore, for the comparison of the accuracy of different techniques, in the paper we solve the 1-D impact problem for which all modes are excited and which has a

very simple analytical solution at short and long observation times. We should also mention that because the computational costs of different space-discretization techniques at the same number of dof are different, then it is necessary to compare the efficiency of these techniques by the estimation of the computational costs at the same accuracy. The findings of the paper can be summarized as follows.

- The two-stage time-integration technique recently suggested in our papers [5,41,42] yields accurate numerical results for elastodynamics problems solved with different space-discretization approaches. For example, due to the spurious oscillations, we have not seen in the literature the accurate numerical solutions of elastodynamics problems at impact

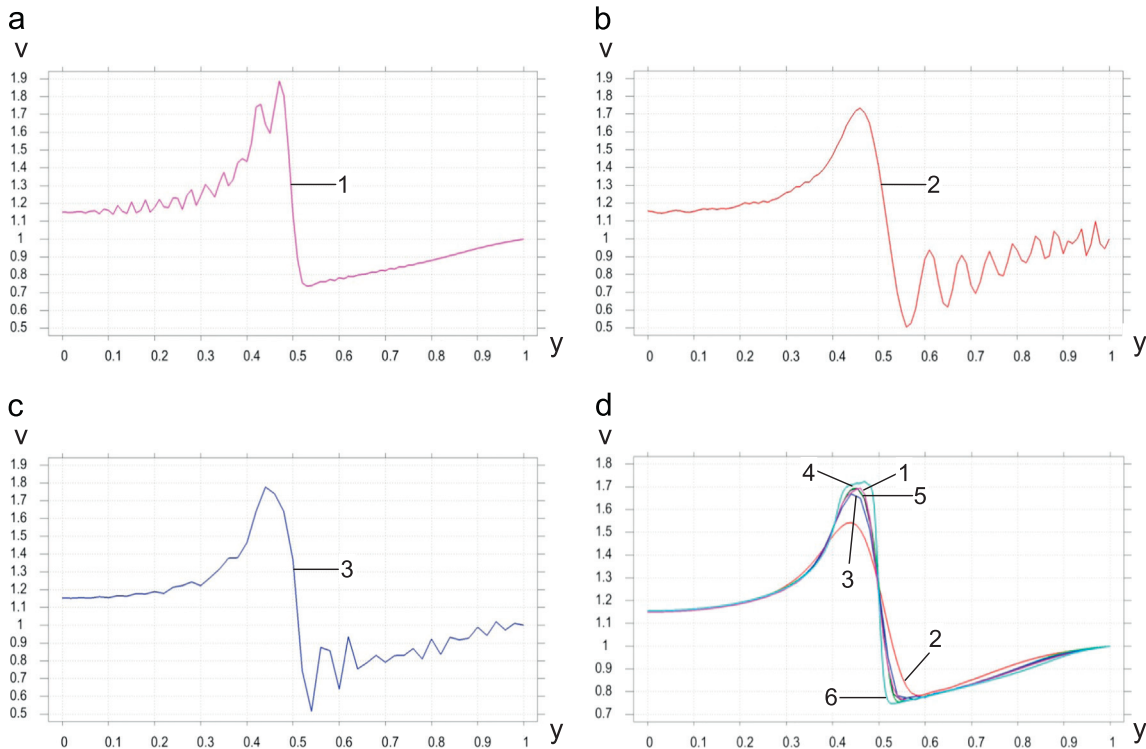


Fig. 30. The velocity distribution along AB at the observation time $T=1.5$ after basic computations (a–c) and after the filtering stage (d). Curves 1, 2, 3, 4, 5 and 6 correspond to the numerical results obtained on uniform meshes with $100 \times 100 = 10,000$ Q4 (reduced dispersion), $100 \times 100 = 10,000$ Q4 (standard), $50 \times 50 = 2500$ Q9 (standard), $300 \times 300 = 90,000$ Q4 (standard), $66 \times 66 = 4356$ Q9 (standard), and $300 \times 300 = 90,000$ Q4 (reduced dispersion) finite elements, respectively.

loading (or high-frequency loading) for the spectral and isogeometric elements as well as for the standard high-order finite elements even in the 1-D case. The applicability of the new approach to different space-discretization techniques considered in the paper is based on the fact that for all these techniques, lower frequencies are resolved more accurately than higher frequencies. Then, by the quantification of the inaccurate high frequencies (in terms of the coefficients a_1 and a_2 ; see the Appendix) and by their filtering at the filtering stage, we obtain accurate numerical results without the spurious oscillations. The new coefficients a_1 and a_2 determined in the paper (see the Appendix) define different ranges of the spurious (inaccurate) frequencies for different space-discretization methods and are used for the filtering of the spurious oscillations in numerical solutions of the 1-D as well as multi-dimensional elastodynamics problems (see [42,44,49] for the applications of the two-stage time integration technique to multi-dimensional impact and wave propagation problems).

- As expected, at the same number of dof, the increase in the order of the standard finite elements, the spectral elements and the isogeometric elements leads to the increase in the accuracy of numerical results (however, the computational costs of higher-order elements are greater than that of lower-order elements at the same dof).
- Except the known case of the linear elements with the lumped mass matrix, all other space-discretization techniques considered in the paper require small time-increments for time integration at the stage of basic computations. Moreover, the time increments should be decreased with the increase in the observation time. Even if for explicit time-integration methods the time increments close to the stability limit may yield accurate results at a small observation time, the time increments should be significantly decreased with the increase in the observation time. For example, for the 2nd-order time-integration methods, the size of time increments should be inversely proportional to the

square root of the observation time (as predicted by the exact time error estimator developed in our paper [47]; the paper [47] also considers the case of high-order time-integration methods). Similar to explicit time-integration methods, comparably small time increments should be used with implicit time-integration methods for the 1-D impact problem. According to our results, the typical statement in finite element textbooks, that for explicit methods a time increment should be close to the stability limit (e.g., see [1,43]) is not true, because the size of a time increment should depend on the observation time and should be much smaller than the stability limit at large observation times.

- The comparison of the space-discretization techniques based on the non-diagonal mass matrices (used with implicit time-integration methods) shows that at the same number of dof, the isogeometric elements yield more accurate results compared with the standard high-order finite elements and the linear elements with reduced dispersion. However, when we compare the computational costs at the same accuracy, the numerical results show the linear elements with reduced dispersion are more computationally efficient than other space-discretization techniques. We should also mention that compared with the isogeometric 3rd-order elements, the computational efficiency of the linear elements with reduced dispersion decreases with the increase in the observation time.
- The comparison of the space-discretization techniques based on the diagonal mass matrices (used with explicit time-integration methods) shows that at the same number of dof, the spectral high-order elements yield more accurate results compared with the standard linear and quadratic finite elements and the linear elements with reduced dispersion. However, when we compare the computational costs at the same accuracy, the numerical results show the linear elements with reduced dispersion are more computationally efficient than the spectral high-order elements. We should also mention that compared with the spectral 10th-order elements, the computational efficiency of the linear

elements with reduced dispersion decreases with the increase in the observation time.

- It is interesting to note that the size of time increments at the filtering stage of the two-stage time-integration technique (this size is calculated according to Eqs. (A.1)–(A.3) from the Appendix) defines the range of actual frequencies used in numerical solutions and can serve as a quantitative measure for the comparison and the prediction of the accuracy and the computational efficiency of different space-discretization techniques not only for the 1-D problem considered in Section 3 but also for the multidimensional problems (e.g., see Section 4 and our papers [4,42,44]).

The estimation and comparison of accuracy of different space-discretization techniques obtained for impact problems (for which all frequencies of the semi-discrete equations are excited) are also valid for any transient acoustics or elastodynamics problem for which only a part of frequencies of the semi-discrete equations is excited; e.g., see [42]. For example, in our paper [42] we showed that the two-stage time-integration approach can be equally applied to wave propagation problems under impact loading as well as under low- and high-frequency loading (the same range of spurious high-frequencies should be filtered independent of applied loading). We also believe that the comparative study of other space-discretization techniques (similar to that considered in the paper) will help us determine the most computationally efficient technique for elastodynamics and acoustics.

Acknowledgments

The research has been supported in part by the Air Force Office of Scientific Research (contract FA9550-12-1-0324) and by Texas Tech University.

Appendix A. The two-stage time-integration technique with filtering spurious oscillations (see [5,41,42])

In order to filter spurious high-frequency oscillations, numerical dissipation (or artificial damping) is usually introduced for the time integration of Eq. (1). As we showed in our paper [42], the use of a time-integration method with numerical dissipation (or artificial damping) at each time increment leads to inaccurate numerical results for low frequencies as well, especially for a long-term integration. It is also unclear in this case how to select the amount of numerical dissipation and to determine the range of spurious high-frequencies to be filtered.

To resolve these issues, we have developed the two-stage time-integration technique (see [5,41,42]) with the stage of basic computations and the filtering stage. This technique is based on the fact that for linear elastodynamics problems, there is no necessity to filter spurious oscillations at each time increment because the errors in high-frequencies do not affect the accuracy of low-frequencies during time integration; see [42]. In the current paper, in basic computations we use the implicit trapezoidal rule or the standard explicit central-difference time-integration method (without numerical dissipation or artificial viscosity) in order to obtain an accurate solution of the semi-discrete elastodynamics problem, Eq. (1) (this solution contains spurious high-frequency oscillations). We should mention that other known implicit and explicit time-integration methods can also be used in basic computations. For the filtering of spurious oscillations, the implicit time-continuous Galerkin (TCG) method with large numerical dissipation developed in [42] (see also Appendix B) is used at the filtering stage with $N=10$ uniform time increments

(5 positive plus 5 negative time increments). This means that there is no real time integration at the filtering stage (the sum of 10 time increments used at the filtering stage is zero). As shown in [42], this time integration is equivalent to the multiplication of each velocity and displacement of the uncoupled system of the semi-discrete equations by a factor of

$$\left(\frac{(3+m)^2 + \Omega^2}{(3+m)^2 + (2+m)^2 \Omega^2} \right)^5$$

(where $\Omega = \omega_j \Delta t$ and ω_j are the eigen-frequencies of the semi-discrete system, Δt is the time increment as well as $m=15$ is used) and does not require the modal decomposition and the calculation of eigen-frequencies. As can be seen, this factor is close to zero for large Ω and is close to unity for small Ω . The size Δt of time increments at the filtering stage indirectly defines the amount of numerical dissipation and the range of spurious oscillations and is calculated according to the following formulas (for uniform meshes)

$$\Delta t = \alpha \left(\frac{c_o T}{dx} \right) \frac{dx \Omega_{0.1}(N)}{c_o}, \quad (\text{A.1})$$

with

$$\alpha \left(\frac{c_o T}{dx} \right) = a_1 \left(\frac{c_o T}{dx} \right)^{a_2}, \quad (\text{A.2})$$

in the 1-D case and

$$\begin{aligned} \Delta t &= \max_j \left[\alpha \left(\frac{c_o T}{dx_j} \right) \frac{dx_j}{c_o} \right] \Omega_{0.1}(N) \\ &= \max_j \left[\frac{dx_j}{c_o} \right]^{1-a_2} a_1 T^{a_2} \Omega_{0.1}(N) \\ &= \left[\frac{dx_{\max}}{c_o} \right]^{1-a_2} a_1 T^{a_2} \Omega_{0.1}(N), \end{aligned} \quad (\text{A.3})$$

for acoustic waves in the 2-D and 3-D cases (see also our papers [5,42]). Here, c_o is the wave velocity; dx is the size of a finite element in the 1-D case; T is the observation time; $dx_{\max} = \max_j dx_j$ is the maximum dimension of finite elements along the axes x_j ($j=1,2$ for 2-D problems and $j=1,2,3$ for 3-D problems); $\Omega_{0.1}(N=10)=0.81$ for the TCG method with $N=10$ time increments. Using the calibration procedure described in [5], we determined the coefficients a_1 and a_2 for the different space-discretization techniques that are presented in Table 1. These coefficients a_1 and a_2 are calibrated in the 1-D case for the filtering of numerical results obtained in basic computations with very small time increments. Eq. (A.3) is based on Eqs. (A.1) and (A.2) with the selection of the maximum size of a time increment with respect to the maximum size of a finite element along the coordinate axes. In contrast to the 2-D and 3-D elastodynamics problems with the compressional and shear waves propagating with different wave velocities and considered in [5,42], acoustic waves propagate with the same velocity c_o in the multi-dimensional case. This simplifies Eq. (A.3) compared with that in [5,42].

We should mention that the filtering stage can be applied in the beginning of calculations as a pre-processor, in the end of calculations as a post-processor or at some intermediate time (see [42,44,46,49] for numerous 1-D, 2-D and 3-D examples of the application of the two-stage time-integration technique).

Appendix B. The implicit TCG method for the filtering stage (see [42])

The method is based on the linear approximations of displacements $\mathbf{U}(t)$ and velocities $\mathbf{V}(t)$ within a time step Δt ($0 \leq t \leq \Delta t$)

(see [42]):

$$\mathbf{U}(t) = \mathbf{U}_0 + \mathbf{U}_1 t, \quad \mathbf{V}(t) = \mathbf{V}_0 + \mathbf{V}_1 t, \quad (\text{B.1})$$

and has the first order of accuracy. Here \mathbf{U}_0 and \mathbf{V}_0 are the known initial nodal displacements and velocities, and the unknown nodal vector \mathbf{V}_1 can be expressed in terms of the unknown nodal vector \mathbf{U}_1 as follows:

$$\mathbf{V}_1 = \frac{1}{a_1} \mathbf{U}_1 - \frac{1}{a_1} \mathbf{V}_0. \quad (\text{B.2})$$

Finally, the following system of algebraic equations is solved in order to determine \mathbf{U}_1 :

$$(\mathbf{M} + a_1^2 \mathbf{K}) \mathbf{U}_1 = -a_1 \mathbf{K} \mathbf{U}_0 + \mathbf{M} \mathbf{V}_0 + \mathbf{R}_1, \quad (\text{B.3})$$

$$a_1 = \frac{m+2}{m+3} \Delta t,$$

$$\mathbf{R}_1 = \frac{(m+2)^2}{(m+3)\Delta t^{m+1}} \int_0^{\Delta t} \mathbf{R}(t) t^{m+1} dt. \quad (\text{B.4})$$

After the calculation of \mathbf{U}_1 from Eq. (B.3), vectors $\mathbf{U}(\Delta t)$ and $\mathbf{V}(\Delta t)$ at the end of a time increment Δt are calculated using Eqs. (B.1) and (B.2) for $t = \Delta t$:

$$\mathbf{U}(\Delta t) = \mathbf{U}_0 + \mathbf{U}_1 \Delta t, \quad \mathbf{V}(\Delta t) = \mathbf{V}_0 + \mathbf{V}_1 \Delta t. \quad (\text{B.5})$$

The parameter m (see Eq. (B.4)) is responsible for the amount of numerical dissipation and is taken $m=15$, see [42].

References

- [1] K.J. Bathe, Finite Element Procedures, Prentice-Hall Inc., Upper Saddle River, New Jersey, 1996.
- [2] T.J.R. Hughes, The Finite Element Method: Linear Static and Dynamic Finite Element Analysis, Prentice-Hall, Englewood Cliffs, NJ, 1987.
- [3] O.C. Zienkiewicz, R.L. Taylor, The Finite Element Method, Butterworth-Heinemann, Oxford, UK, 2000.
- [4] A.V. Idesman, D. Pham, Finite element modeling of linear elastodynamics problems with explicit time-integration methods and linear elements with the reduced dispersion error, Comput. Methods Appl. Mech. 271 (2014) 86–108.
- [5] A.V. Idesman, H. Samajder, E. Aulisa, P. Seshaiyer, Benchmark problems for wave propagation in elastic materials, Comput. Mech. 43 (6) (2009) 797–814.
- [6] S. Krenk, Dispersion-corrected explicit integration of the wave equation, Comput. Methods Appl. Mech. Eng. 191 (2001) 975–987.
- [7] K.J. Marfurt, Accuracy of finite difference and finite element modeling of the scalar and elastic wave equation, Geophysics 49 (1984) 533–549.
- [8] R. Mullen, T. Belytschko, Dispersion analysis of finite element semidiscretizations of the two-dimensional wave equation, Int. J. Numer. Methods Eng. 18 (1982) 11–29.
- [9] B. Yue, M.N. Guddati, Dispersion-reducing finite elements for transient acoustics, J. Acoust. Soc. Am. 118 (4) (2005) 2132–2141.
- [10] M. Ainsworth, H.A. Wajid, Optimally blended spectral-finite element scheme for wave propagation and nonstandard reduced integration, SIAM J. Numer. Anal. 48 (1) (2010) 346–371.
- [11] F. Casadei, E. Gabellini, G. Fotia, F. Maggio, A. Quarteroni, A mortar spectral/finite element method for complex 2d and 3d elastodynamic problems, Comput. Methods Appl. Mech. Eng. 191 (45) (2002) 5119–5148.
- [12] D. Komatitsch, C. Barnes, J. Tromp, Simulation of anisotropic wave propagation based upon a spectral element method, Geophysics 65 (4) (2000) 1251–1260.
- [13] D. Komatitsch, J.-P. Vilotte, Spectral element method: an efficient tool to simulate the seismic response of 2d and 3d geological structures, Bull. Seismol. Soc. Am. 88 (2) (1998) 368–392.
- [14] D. Komatitsch, J.-P. Vilotte, R. Vai, J.M. Castillo-Covarrubias, F.J. Sanchez-Sesma, The spectral element method for elastic wave application to 2-d and 3-d seismic problems, Int. J. Numer. Methods Eng. 45 (9) (1999) 1139–1164.
- [15] C. Pozrikidis, Introduction to Finite and Spectral Element Methods Using MATLAB, CRC Press, 2005.
- [16] D.J. Benson, Y. Bazilevs, E. De Luycker, M.-C. Hsu, M. Scott, T.J.R. Hughes, T. Belytschko, A generalized finite element formulation for arbitrary basis functions: from isogeometric analysis to XFEM, Int. J. Numer. Methods Eng. 83 (6) (2010) 765–785.
- [17] D. Benson, Y. Bazilevs, M.-C. Hsu, T. Hughes, A large deformation, rotation-free, isogeometric shell, Comput. Methods Appl. Mech. Eng. 200 (13–16) (2011) 1367–1378.
- [18] J. Cottrell, A. Reali, Y. Bazilevs, T. Hughes, Isogeometric analysis of structural vibrations, Comput. Methods Appl. Mech. Eng. 195 (41–43) (2006) 5257–5296.
- [19] T. Hughes, A. Reali, G. Sangalli, Duality and unified analysis of discrete approximations in structural dynamics and wave propagation: comparison of p-method finite elements with k-method NURBS, Comput. Methods Appl. Mech. Eng. 197 (49–50) (2008) 4104–4124.
- [20] L.C. Wrobel, M.H. Aliabadi, The Boundary Element Method, Wiley, 2002.
- [21] K.T. Danielson, S. Hao, W.K. Liu, R.A. Uras, S. Li, Parallel computation of meshless methods for explicit dynamic analysis, Int. J. Numer. Methods Eng. 47 (7) (2000) 1323–1341.
- [22] H. Li, Meshless Methods and their Numerical Properties, CRC Press, 2013.
- [23] S. Li, W.K. Liu, Moving least-square reproducing kernel method part II: Fourier analysis, Comput. Methods Appl. Mech. Eng. 139 (1–4) (1996) 159–193.
- [24] S. Li, W.K. Liu, Reproducing kernel hierarchical partition of unity, part II—applications, Int. J. Numer. Methods Eng. 45 (3) (1999) 289–317.
- [25] G.R. Liu, Meshfree Methods: Moving Beyond the Finite Element Method, CRC Press, 2009.
- [26] W.K. Liu, Y. Chen, R. Uras, C.T. Chang, Generalized multiple scale reproducing kernel particle methods, Comput. Methods Appl. Mech. Eng. 139 (1–4) (1996) 91–157.
- [27] G. Liu, K. Dai, T. Nguyen, A smoothed finite element method for mechanics problems, Comput. Mech. 39 (6) (2007) 859–877.
- [28] G. Liu, T. Nguyen, K. Dai, K. Lam, Theoretical aspects of the smoothed finite element method (SFEM), Int. J. Numer. Methods Eng. 71 (8) (2007) 902–930.
- [29] I. Babuska, F. Ihlenburg, T. Strouboulis, S.K. Gangaraj, Posteriori error estimation for finite element solutions of helmholtz' equation—part II: estimation of the pollution error, Int. J. Numer. Methods Eng. 40 (21) (1997) 3883–3900.
- [30] I. Babuska, T. Strouboulis, S.K. Gangaraj, C.S. Upadhyay, Pollution error in the h-version of the finite element method and the local quality of the recovered derivatives, Comput. Methods Appl. Mech. Eng. 140 (1–2) (1997) 1–37.
- [31] A. Deraemaeker, I. Babuska, P. Bouillard, Dispersion and pollution of the FEM solution for the Helmholtz equation in one, two and three dimensions, Int. J. Numer. Methods Eng. 46 (4) (1999) 471–499.
- [32] H.P. Cherukuri, Dispersion analysis of numerical approximations to plane wave motions in an isotropic elastic solid, Comput. Mech. 25 (4) (2000) 317–328.
- [33] W. Dauksher, A.F. Emery, Solution of elastostatic and elastodynamic problems with Chebyshev spectral finite elements, Comput. Methods Appl. Mech. Eng. 188 (1) (2000) 217–233.
- [34] D. Gabriel, J. Plesek, R. Kolman, F. Vales, Dispersion of elastic waves in the contact-impact problem of a long cylinder, J. Comput. Appl. Math. 234 (2010) 1930–1936.
- [35] G. Seriani, S.P. Oliveira, Optimal blended spectral-element operators for acoustic wave modeling, Geophysics 72 (5) (2007) 95–106.
- [36] G. Seriani, S.P. Oliveira, Dispersion analysis of spectral element methods for elastic wave propagation, Wave Motion 45 (6) (2008) 729–744.
- [37] S. Cho, H. Huh, K. Park, A time-discontinuous implicit variational integrator for stress wave propagation analysis in solids, Comput. Methods Appl. Mech. Eng. 200 (5–8) (2011) 649–664.
- [38] E.G. Dutra Do Carmo, C. Da Silva Garcia Monteiro, W.J. Mansur, A finite element method based on capturing operator applied to wave propagation modeling, Comput. Methods Appl. Mech. Eng. 201–204 (2012) 127–138.
- [39] L. Maheo, V. Grolleau, G. Rio, Numerical damping of spurious oscillations: a comparison between the bulk viscosity method and the explicit dissipative Tchaumala-Wielgosz scheme, Comput. Mech. 51 (1) (2013) 109–128.
- [40] K. Park, S. Lim, H. Huh, A method for computation of discontinuous wave propagation in heterogeneous solids: basic algorithm description and application to one-dimensional problems, Int. J. Numer. Methods Eng. 91 (6) (2012) 622–643.
- [41] A.V. Idesman, A new high-order accurate continuous Galerkin method for linear elastodynamics problems, Comput. Mech. 40 (2007) 261–279.
- [42] A.V. Idesman, Accurate time integration of linear elastodynamics problems, Comput. Model. Eng. Sci. 71 (2) (2011) 111–148.
- [43] R.D. Cook, D.S. Malkus, M.E. Plesha, R.J. Witt, Concepts and Applications of Finite Element Analysis, Wiley, 2001.
- [44] A. Idesman, M. Schmidt, J.R. Foley, Accurate finite element modeling of linear elastodynamics problems with the reduced dispersion error, Comput. Mech. 47 (2011) 555–572.
- [45] G.M. Hubert, T.J.R. Hughes, Space-time finite element methods for second-order hyperbolic equations, Comput. Methods Appl. Mech. Eng. 84 (3) (1990) 327–348.
- [46] A. Idesman, K. Subramanian, M. Schmidt, J.R. Foley, Y. Tu, R.L. Sierakowski, Finite element simulation of wave propagation in an axisymmetric bar, J. Sound Vib. 329 (2010) 2851–2872.
- [47] A.V. Idesman, A new exact, closed-form a priori global error estimator for second- and higher-order time integration methods for linear elastodynamics, Int. J. Numer. Methods Eng. 88 (2011) 1066–1084.
- [48] A.V. Idesman, D. Pham, Accurate finite element modeling of acoustic waves, Comput. Phys. Commun. 185 (7) (2014) 2034–2045.
- [49] A. Idesman, M. Schmidt, J.R. Foley, Accurate 3-d finite element simulation of elastic wave propagation with the combination of explicit and implicit time-integration methods, Wave Motion 48 (2011) 625–633.